The onset and regulation of star-formation in the lowest mass dark matter halos

by

Matthew Pereira Wilson
B.Sc., University of Waterloo, 2020

A Thesis Submitted in Partial Fulfillment of the
Requirements for the Degree of

MASTER OF SCIENCE

in the Department of Physics and Astronomy

The onset and regulation of star-formation in the lowest mass dark matter halos

by

Matthew Pereira Wilson
B.Sc., University of Waterloo, 2020

Supervisory Committee

Dr. Julio Navarro, Supervisor
(Department of Physics and Astronomy)

Dr. Ruobing Dong, Departmental Member
(Department of Physics and Astronomy)

ABSTRACT

We use the APOSTLE suite of cosmological simulations to examine the role of the cosmic ionizing background in regulating star formation (SF) in low-mass LCDM halos. In agreement with earlier work, we find that, after reionization, SF can only proceed in halos whose mass exceeds a redshift-dependent "critical" virial mass determined by the structure of LCDM halos and the thermal pressure of UV-heated gas. This critical mass increases from $M_{\rm crit} \sim 10^8\,M_\odot$ at $z \sim 11$ to $\sim 10^{9.7}\,M_\odot$ at $z = 0$, roughly following the average mass growth history of halos in that mass range. This implies that most halos above or below critical at present have remained so since early times. In particular, the halos of most galaxies today were already above-critical (and thus forming stars) at high redshift, providing a simple explanation for the ubiquitous presence of ancient stellar populations in dwarfs, regardless of luminosity. It also implies that $M_{\rm crit}$ today represents a "threshold" mass below which the fraction of "dark" halos increases steeply. Sub-critical halos may still host luminous galaxies if they were above-critical at some point in the past. SF ceases if a halo falls into the sub-critical regime; depending on each halo's accretion history this can occur over a wide range of times, explaining why SF in many dwarfs seems to continue well past the reionization epoch. It also suggests a tantalizing explanation for the episodic nature of SF in some dwarfs, which, in this interpretation, would be linked to temporary halo excursions above and below the critical boundary. In the simulations, $M_{\rm crit}(z)$ cleanly separates star-forming from non-star-forming systems at all redshifts, indicating that the ionizing UV background, and not stellar feedback, is what regulates the beginning and the end of SF in the faintest dwarfs. Galaxies in sub-critical halos should make up a sizable population of faint field dwarfs, distinct from those in more massive halos because of their lack of ongoing star formation. Although few such galaxies are known at present, the discovery of this population would provide strong support for our results.

Contents

List of Figures

ACKNOWLEDGEMENTS

I would like to thank:

the stable climate, for allowing civilization to flourish.

my parents, Jonathan and Cristina, for setting me on the right track,

and Shoshannah, for pushing me past the finish line.

Julio, for guiding my journey in Astronomy.

Isabel and Alejandro, for insightful discussion and advice.

Lucy, my dog, for snoring during my work hours.

DEDICATION

that we may, one day, understand the Universe, and its beauty.

Chapter 1

Introduction

1.1 The LCDM Universe

The standard model of cosmology is currently the Λ Cold Dark Matter model (henceforth LCDM), which describes a spatially flat universe with an accelerating rate of expansion at present. Large scale observations of galaxy clustering (baryon acoustic oscillations, eg. Percival et al. 2010) and of the Cosmic-Microwave-Background (CMB) have placed stringent constraints on the mass-energy composition of the universe. The latest Planck Collaboration et al. (2020) survey estimates that the Universe is composed of approximately 1/3 matter and 2/3 dark-energy. Dark-energy, or Λ - Einstein's cosmological constant - is needed to explain the universe's increasing rate of expansion. Of the Universe's matter component, the vast majority ($\sim 83\%$) exists in the form of Cold Dark Matter (CDM), a non-luminous and collisionless type of massive particle whose existence is not accounted for by the Standard Model of Particle Physics. However, the existence of some invisible particle seems necessary to explain the large, but otherwise unaccounted for, gravitational effect observed on all galactic and cosmological scales. Some examples are the rotation curves and stellar velocity dispersions of galaxies (eg. Rubin and Ford 1970), measurements of gravitational lensing (eg. Clowe et al. 2006), and the presence of hot gas in clusters (eg. Evrard et al. 1996), which all suggest the existence of dark matter.

In the LCDM paradigm, structure is formed from the gravitational collapse of overdense regions. Structure formation is driven primarily by the collapse of dark matter, which decoupled from radiation prior to baryonic matter due to its collisionless nature, via the formation of dark matter halos. The gravitational potentials

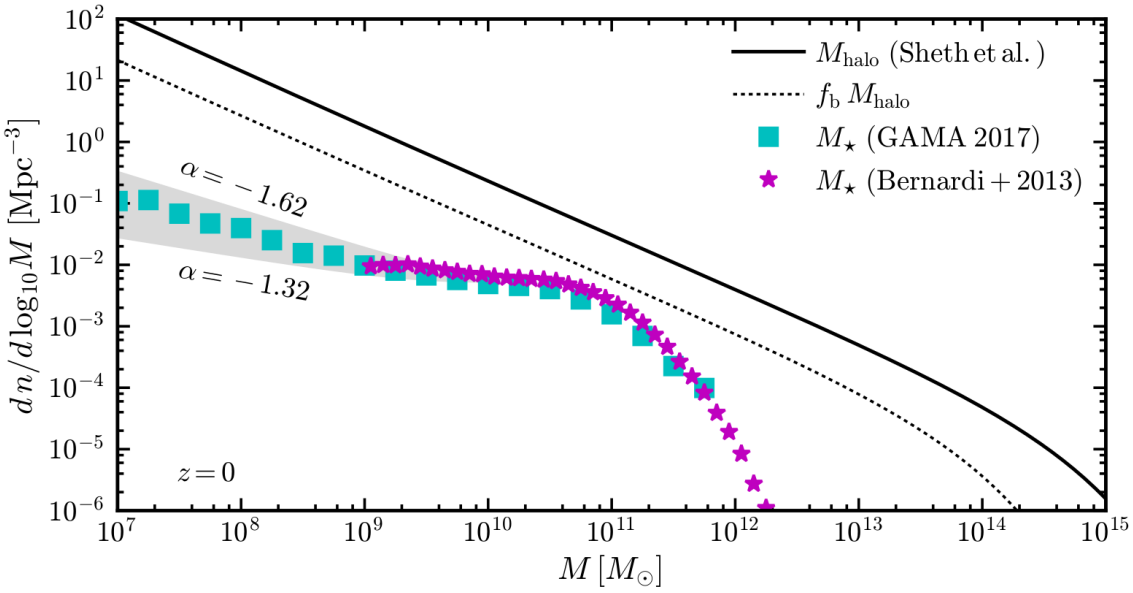

Figure 1.1: Stellar-mass and halo-mass functions. Halo mass function is shown as solid-black line, with corresponding mass in baryon (assuming universal fraction, f_b) in doted-black line. Stellar mass functions from two sources shown as magenta stars and cyan squares. Taken from Bullock and Boylan-Kolchin (2017).

formed by the early collapse of dark matter halos act as the "seeds" in which gas (ie. baryons) would later collapse into and begin forming stars. It is expected that all galaxies formed this way, at the centre of dark matter halos.

However, galaxies and their dark matter halos continue to grow, hierarchically, merging and accreting smaller neighbours (see, eg. White and Rees 1978; White and Frenk 1991; Bullock et al. 2001). The central regions of accreted dark matter halos, and the stellar populations at their centre, are sufficiently bound to remain in orbit within the larger halo. Evidence of this hierarchical growth is present in the rich substructures observed on all scales today eg., the clustering of galaxies, and the satellites of the Milky Way.

1.1.1 Stellar mass to halo mass relation

The shared growth history of dark matter halos and galaxies begets the existence of a stellar mass-to-halo mass relation (SMHM). This relation can be probed via observations, where the stellar mass may be calculated from the total light emitted by a galaxy. However, it is particularly challenging to estimate the total mass of the

dark matter halo, which extends well beyond the region usually traced by baryons. Observational techniques for the most massive halos can usually rely on gravitational lensing, X-ray emission of hot intra-cluster gas, or the orbital dynamics of satellite galaxies, which are used to infer the total enclosed mass in clusters of galaxies. For lower mass structures, observations rely on the velocity dispersion of stars and rotation curves of gas to estimate the enclosed mass, but these observations can only probe the inner regions of the dark matter halo. In order to estimate the total dark matter mass, some assumption is needed for the distribution of dark matter beyond that region.

Given the observational difficulties in estimating the dark matter mass of the majority of astronomical objects, a complete SMHM relation relies on a theoretical halo-mass function to track the distribution and abundance of dark matter halos down to very low masses. This halo mass function can be derived from cosmological simulations (eg. Moster et al. 2010), or from the analytical Press and Schechter (1974) formalism (eg. Murray et al. 2013). The typical method of relating the observed stellar masses to the theoretical halo mass function is known as abundance matching, whereby the most massive dark matter halos are assigned (on average) to the most massive system in stellar mass. This abundance matching technique produces results in line with observational evidence (eg. Behroozi et al. (2010) in the $10^{11} - 10^{15} M_{\odot}$ mass range, and Read et al. (2017) in the low mass range $\sim 10^{9} M_{\odot}$).

In detail, the conversion between stellar mass and halo mass is non linear due to the variation in efficiency with which halos transform their available gas into stars. The stellar mass function (from observations; star and square symbols) and a halo mass function (theoretical; solid black line) are shown in Fig. 1.1, taken from Bullock and Boylan-Kolchin (2017). Star-formation efficiency peaks for galaxies of stellar mass $M_{*} \sim 10^{11} M_{\odot}$, which, via abundance-matching, typically inhabit a dark matter halo of $\sim 10^{12} M_{\odot}$. For masses above this *characteristic mass*, supermassive black-hole feedback (ie. active galactic nuclei; AGN) are expected to play an increasingly dominant role at preventing further star-formation, and contribute to the sharp decline in the stellar mass function. For lower masses, stellar feedback and the photo-ionizing UV-background are the main processes reducing star-formation efficiency.

The diverging shapes of the stellar mass and halo mass functions towards lower masses are in tension with the expectation that all dark matter halos should host a galaxy (ie. abundance matching). The total number of low mass galaxies observed does not match with the total number of dark matter halos expected. This problem

extends to the number of dark matter substructures expected in orbit around the Milky Way galaxy, an issue commonly referred to as the "Missing Satellites" problem (Klypin et al. 1999; Moore et al. 1999a).

The solution to this problem requires that dark matter halos become significantly inefficient at forming stars towards lower masses, with the existence of a minimum mass below which dark matter halos cannot host star-formation. The process generally understood to stop star-formation in halos below some minimum mass is the photo-ionizing UV background (see, eg. Efstathiou 1992; Bullock et al. 2000; Benson et al. 2002).

1.1.2 Cosmic timeline: the epoch of reionization

In the LCDM model of cosmology, the inter-galactic medium (IGM) underwent a transition in its ionization state after the first galaxies formed. This transition, from neutral to ionized, is understood to have had a significant impact on the process of star-formation in the shallowest dark matter potentials (eg. Couchman and Rees 1986; Chiba and Nath 1994; Shapiro et al. 1994).

Neutral gas formed approximately $\sim 370,000$ yrs after the Big-Bang, around redshift $z \sim 1100$, when the Universe had expanded and cooled to $\sim 3,000$ K. The formation of neutral atoms marks the decoupling of baryons from the radiation field (known as the epoch of decoupling), which allowed for gas to cool radiatively and begin accreting into dark matter halos. This also corresponds to the time when the Cosmic Microwave Background (CMB) formed.

Star formation begins once gas inside dark matter halos reaches a high enough density to become self-gravitating and collapse. For this, the gas needs to lose the thermal energy it gained during its gravitational collapse via radiation (eg. Tegmark et al. 1997). The properties of the first stars are still being debated (see, eg. Barkana and Loeb 2001; Bromm and Yoshida 2011, for a review), but given that the cooling mechanisms available for primordial gas were particularly inefficient, due to the lack of elements heavier than Helium, it is expected that the first stars were quite massive, $\sim 100 M_{\odot}$, and short lived (eg. Omukai and Palla 2003). Due to their size, and high surface temperatures, they emitted large amounts of UV-radiation which were initially absorbed by the neutral gas in the IGM, beginning the process of re-ionization of the Universe (eg. Ricotti et al. 2001).

The Epoch of Reionization (EOR) in practice began as ionized *bubbles* of gas

surrounding the first structures that assembled, around $z \sim 30$, which grew over-time and started overlapping with the ionized *bubbles* of other nearby structures (eg. Dawoodbhoy et al. 2018). Eventually, the radiation of young blue stars, subsequent supernovae, and quasars (black-hole accretion disk) ionized all the inter-galactic gas, a process that is understood to have been complete by $z \sim 6$ (eg. Mortlock et al. 2011). After reionization, the Universe is still permeated by a nearly spatially uniform photo-ionizing background.

The reionization of the Universe also heated the gas in the IGM to $\sim 10^4$ K. This heating increased the pressure of gas in the IGM, effectively preventing gas from collapsing into the shallowest potential wells, and suppressing the accretion of gas inflows to halos whose virial temperature[1] is below that of the IGM (Quinn et al. 1996; Thoul and Weinberg 1996; Navarro and Steinmetz 1997). This process would eventually stop halos below a certain mass from forming new stars, as they are cut-off from new gas supplies. Additionally, it also prevented star formation from beginning in low-mass halo that assembles after reionization, which why it is the commonly proposed solution to the "Missing Satellites" problem. The exact details of this minimum halo mass are the main focus of this thesis, and will be covered in more detail in section 3.1.

1.2 Dwarf galaxies

Dwarf galaxies inhabit the lowest mass dark matter structures and sub-structures in the Universe. They are the most numerous population of galaxies but, due to their small size and luminosity, the catalog of dwarfs within the Local Group is likely still incomplete (eg. Fattahi et al. 2016). However, as was hinted at in section 1.1.2, the shallowness of their dark matter potentials make them particularly sensitive to the baryonic processes that drive galaxy formation and evolution.

In their abundance and diversity, dwarf galaxies also probe a wide range of environmental factors. Some of them evolve in near isolation, making them ideal to study the internal processes of star formation, stellar feedback, and the impact of the photo-ionizing background. Others have been accreted into the potential well of more

[1] Temperature at the virial radius. We define the virial radius, r_{200}, of each halo as that enclosing a region of mean density equal to $200\times$ the critical density for closure, $\rho_{\rm crit} = 3H(z)^2/8\pi G$, where $H(z)$ is Hubble's "constant". We denote values computed within or at the virial boundary with a "200" subscript.

massive systems, such as the Milky Way or Andromeda, which can be used to study the effects of tidal (Mayer et al. 2001; Kravtsov et al. 2004; Fattahi et al. 2018) and ram-pressure (Gunn and Gott 1972; Abadi et al. 1999) forces.

Traditionally, dwarf galaxies have been classified based on their morphology, current level of star-formation, and the presence of molecular gas. Broadly, the three categories are: dwarf spheroidal (dSph) with no gas or recent star formation, dwarf Irregular (dIrr) with some gas and new star-formation (Hodge 1971), and 'transitional' systems (dT), which have had recent star-formation, but no gas remaining (see the review by Tolstoy et al. 2009, and references therein).

1.2.1 Star Formation in dwarfs

Dwarf galaxies show an astonishing variety of star-formation histories (Weisz et al. 2011, 2014a,b; Gallart et al. 2015; Skillman et al. 2017), which is broadly attributed to the varying effects that the photo-ionizing background, stellar feedback, and environmental factors can have on the cooling of gas in the shallow gravitational potentials of low mass halos. However, the details of how these mechanisms come together to produce the diversity of star-formation histories is still not fully understood.

A possible way to study the effects of reionization is by examining the imprint it may have left on the star-formation history of galaxies (eg. Ricotti and Gnedin 2005). It is expected that reionization sharply truncated the star-formation-history of the faintest dwarfs, the most extreme of which may be identified today as "fossils", having formed their entire stellar population prior to reionization. Some fossil dwarfs, satellites of the Milky Way, may have already been identified, supporting this hypothesis (eg. Brown et al. 2014). However, recovering the halo masses of these galaxies, and therefore the halo mass at which these processes become dominant, are significantly more difficult, given that satellite galaxies have likely been tidally stripped.

There is also evidence that dwarf galaxies can have multiple phases of star formation, intermediated by long periods of quiescence, suggesting that the impact of reionization for some halo masses may be more nuanced than simple truncation (Weisz et al. 2014b). For example, Ricotti (2009) propose that dark matter halos which stop accreting gas at reionization may still host new star formation at later times, due to the increase in concentration of dark matter halos and the evolution of the temperature of intergalactic gas over cosmic time. Confirming that this regulation of star formation in dwarf galaxies can be caused by the photo-ionizing background will

require a more detailed understanding of the halo mass at which star formation can occur.

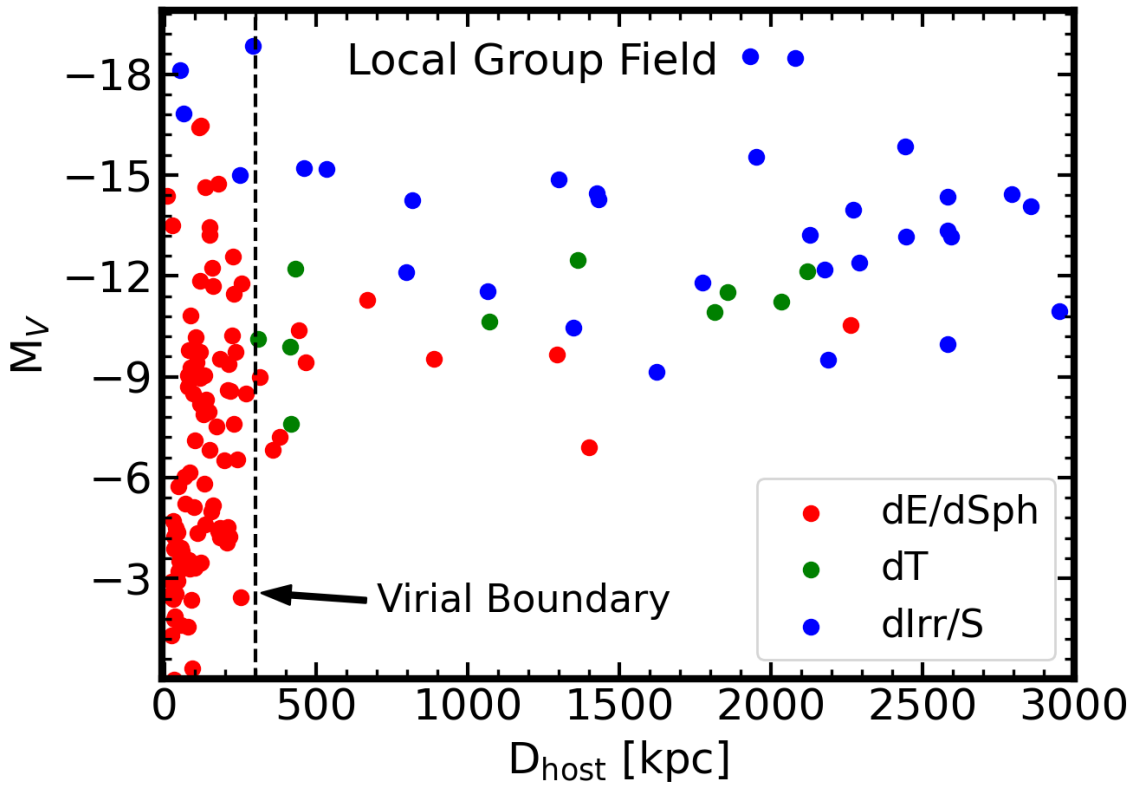

Figure 1.2: Morphological classification of Local Group dwarf galaxies, as a function of absolute V-band magnitude (M_V) and distance from nearest massive galaxy (Andromeda or Milky Way). Galaxies at distances smaller than 300 kpc to either the Milky Way or Andromeda ($D_{\rm host} < 300$ kpc) are considered satellite galaxies, while everything outside that radius is a field galaxy.

1.2.2 Environmental quenching

A complicating factor in disentangling the effect of reionization on the star formation properties of dwarf galaxies is the effect that environment can play. Dwarf galaxies within the virial radius of either the Milky Way or Andromeda galaxy are more likely to be quiescent and lack the gas to form new stars (dE/dSph), compared to galaxies in the field, the region of the Local Group outside the virial radii of the Milky Way and Andromeda galaxies. This is because field galaxies are significantly less likely to have been affected by tidal or ram-pressure forces, which typically strip gas from galaxies and inhibit star-formation.

A simple picture of the cumulative effect that environment can have on the present day star formation of dwarf galaxies can be gathered from their morphological classification. This trend is shown in Fig. 1.2, with the morphological classification of Local Group galaxies taken from the McConnachie (2012) catalog[2]. Galaxies within the virial radii of their host, $\sim$ 300 kpc for the Milky Way or Andromeda (eg. Watkins et al. 2010), are largely quiescent (dE/dSph). There are some exceptions to this rule, particularly the most massive systems, with Triangulum, LMC, SMC, and IC10 (named in order of decreasing M_V) all hosting new star-formation today.

Beyond the virial radius, survey's detection limits significantly reduce the number of galaxies observed with lower luminosities. However, it is apparent that the majority of field dwarf galaxies are currently experiencing new star-formation, in contrast to satellite galaxies of the Milky Way and Andromeda in the same absolute magnitude range ($-15 < M_V < -9$). Early SDSS observations of isolated dwarf galaxies also suggested that all field dwarf galaxies should be star forming (Geha et al. 2012). However, there are some quiescent galaxies in the field as well, but it is not fully understood how they became so. Cetus and Tucana, in particular, may have been quenched environmentally on passage through the Milky Way halo, but then ejected back into the field via a multiple-body interaction (Sales et al. 2007; Teyssier et al. 2012). The possibility remains that other quenched galaxies in the field have also been quenched via this mechanism - so called back-splash galaxies (Balogh et al. 2000; Gill et al. 2005).

Alternatively, a minimum halo mass that can host star-formation, imposed by the hot IGM and photo-ionizing background, may also play a role in explaining the diversity of star formation rates for dwarf galaxies in the field today, explaining why only the lowest mass field dwarfs are quiescent. These quiescent field dwarfs are therefore promising candidates for studying the photo-ionizing background, and the structure of low-mass dark matter halos.

1.3 Thesis Outline

In this project we use an analytical model to describe the onset of star formation in the lowest mass dark matter halos, and compare our results to the APOSTLE suite of cosmological simulations (eg. Fattahi et al. 2016; Sawala et al. 2016). We use a

[2] https://www.cadc-ccda.hia-iha.nrc-cnrc.gc.ca/en/community/nearby/

version of the "critical mass" model first described by Benítez-Llambay and Frenk (2020), which assumes the gas in these halos is in hydrostatic equilibrium with the dark matter potential and in thermal equilibrium with the photo-ionizing background. We validate the critical mass predicted by the analytical model at present day with the APOSTLE simulations and against other cosmological simulations.

This thesis is sectioned as follows: Chapter 2 provides a brief overview of cosmological simulations in general, and details about the APOSTLE simulation; Chapter 3 covers previous analytical models that attempted to describe the minimum mass for star formation, and explain the hydrostatic equilibrium model used for this work. Finally, Chapter 4 compares the analytical model results with the APOSTLE simulation, and in Chapter 5 we summarize our conclusions. Most of the results presented in Chapter 4 have also been submitted for publication.

Chapter 2

Cosmological Simulations

Cosmological simulations have been essential for the development of the LCDM model, and our understanding of how galaxies form and evolve within it (see, eg. Frenk and White 2012, for a review). They currently allow us to follow the evolution of the Universe from the initial density fluctuations of the early universe, until present day, with remarkable observational agreement with the morphology, stellar mass, and large-scale distribution of simulated galaxies (eg. Wang et al. 2015; Schaye et al. 2015; Springel et al. 2018).

Simulations have achieved this by recreating the initial, scale-free, matter-density fluctuations, typically around $z \sim 100$, and forward modelling how these fluctuations evolve via the force of gravity and gas hydro-dynamics. Due to the physical and temporal scales involved, simulations are limited in their volume, resolution, and in which physical processes can be directly modelled. For example, gas cooling, the multi-phase inter-stellar medium, star-formation, stellar and black-hole feedback, are all essential for the formation and evolution of galaxies, but since they occur on a scale below the resolution of most simulations, their effects are modelled via the inclusion of "subgrid models". In practice, these "subgrid models" are implemented as physically motivated semi-analytic models, which have a certain number of adjustable parameters. Simulations of large volumes usually rely on a calibration procedure to choose these parameters, via the exploration of the valid parameter space in an attempt to best reproduce some observational constraint. Common observational constraints for the calibration process are the star-formation rate density as a function of cosmic time, the galaxy stellar mass or the stellar-to-halo mass relation at present day. See Somerville and Davé (2015); Vogelsberger et al. (2020) for excellent reviews of cosmological simulations.

On the largest scales, the force of gravity is dominant over any of the baryonic effects. Studies which focus on the distribution of matter, and which were essential to demonstrate the properties of cold dark matter (eg. Springel et al. 2005), can usually be done via N-body simulations, which solve exclusively for the effect of gravity on otherwise collisionless particles. In order to model in detail how galaxies form, it is necessary to include the behaviour of baryons. Unlike stars and dark matter, which are collisionless and therefore affected only by gravity, gas behaves like a collisional fluid, which significantly increases the number of equations, and therefore the computational cost. Hydro simulations are run for smaller volumes than N-body simulations, but with modern supercomputers, they can still model a statistically significant volume, at the expense of either spatial or mass resolution. For example, the EAGLE simulation (Schaye et al. 2015), which follows a volume of 100^3 cMpc^3 until present day, have a mass resolution of baryons and dark matter of $\sim 10^6 M_\odot$. At this resolution, dwarf galaxies of total mass $\sim 10^9 M_\odot$ are sampled by 1000 dark matter and at most 100 gas particles, which is insufficient to resolve their structure, and the onset of star-formation in detail.

Zoom-in simulations can be employed in order to study the evolution of lower-mass objects within a cosmological environment, by increasing the resolution of a simulated region at the expense of reduced volume. The zoom-in region is usually selected from a previously run N-body simulation, whose properties at present day resemble some configuration of interest - eg. a cluster of galaxies with similar mass to the Coma cluster (eg. Katz and White 1993), or the Local Group environment. The simulation volume is then re-run, where only the region which collapsed to form the region of interest, is initialized with baryons and at a higher resolution; the surrounding region is run with N-body particles only, and at a low resolution. This method preserves the gravitational effects of the cosmological environment, while adding the needed resolution in the region of interest. The APOSTLE suite of simulations, described in the following section, are a collection of zoom-in simulations selected to study the properties of the Local Group today.

2.1 The APOSTLE simulations

The APOSTLE[1] simulation suite consists of a set of twelve zoom-in cosmological hydrodynamical simulations. The volumes selected for re-simulation were taken from the DOVE N-body simulation (Jenkins 2013), a 100^3 cMpc^3 box with a particle mass resolution of $8.8 \times 10^6 M_\odot$. The zoom-in regions fully enclose a volume of $\sim 3^3$ cMpc^3 and were chosen so as to recreate the Local Group environment at present day. In particular, they each have a pair of halos with total mass, separation, and kinematic properties similar to those of the Milky Way-Andromeda system. In detail, the main pair had:

- a separation between 600 and 1000 kpc;
- relative radial velocity between -250 and 0 km s^{-1};
- relative tangential velocity less than 100 km s^{-1};
- total virial mass of the two main primaries is $10^{12.2} - 10^{12.6} M_\odot$

and with field dwarfs galaxies with recession velocities similar to those observed for the Local Group (see Fattahi et al. 2016, for full details of the selection procedure).

Fig.2.1 shows one of the APOSTLE volumes, *V1*, in its dark matter (left), gas (middle), and stellar (right) components at present day. The same volume is viewed from two angles, face-on (top), and an edge-on view (bottom), as most of the matter has collapse into a 2-dimensional sheet. This sheet has linear structures of higher density, called filaments, and at the intersection of multiple filaments we see dark matter halos, the sites of galaxy formation. The Milky Way and Andromeda analogs correspond to the central pair of massive halos, with a virial masses of $M_{200} = 1.10 \times 10^{12} M_\odot$, $1.66 \times 10^{12} M_\odot$ respectively, and a separation of 850 kpc. The surrounding region extends out to 3 Mpc around the baryonic centre of the two primaries. In this volume, there is a third massive galaxy to the left of the main pair, which has no Local Group equivalent.

The effects of the heating of the IGM after the epoch of reionization are clearly visible in the comparison between the dark matter and gas panels. The small-scale structure of dark matter is significantly more pronounced than that of the gas, because the hot IGM is unable to collapse into the shallow gravitational potential of the

[1] "A Project Of Simulating The Local Environment"

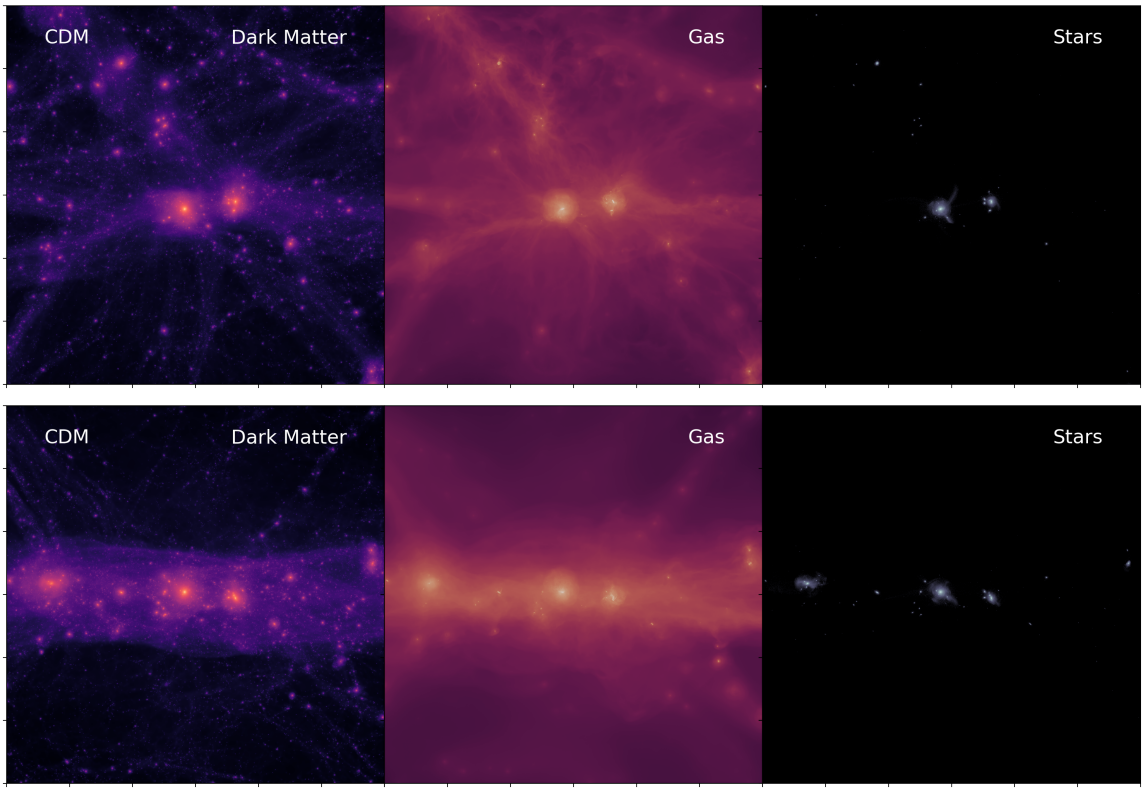

Figure 2.1: Volume 'V1' of the APOSTLE simulation in the highest resolution run (L1), centered on the bary-centre of the Milky Way and Andromeda analogs, extending out to a distance of 3 Mpc. Top panels show the system face-on to the 2D, and the bottom panel show the edge-on view. Dark matter (left), gas (middle) and stellar (star) components were plotted with SPHViewer (Benítez-Llambay 2017).

smallest dark matter halos. This results in a "smoothing out" of overdensities in the gas image, compared to the dark matter, which does not significantly affect the largest dark matter halos; the Milky Way and Andromeda analogs are clear overdensities in the gas and dark matter panels.

The region surrounding the two main primaries is therefore ideal for studying the impact of reionization and the photo-ionizing background on star-formation in shallow dark matter halos, and why the APOSTLE simulations were selected for this study. Studies of the dwarf galaxy population in APOSTLE have been carried out in the past with, for example, Fattahi et al. (2020) finding that the number of field dwarf galaxies out to 3 Mpc may outnumber the number of satellites of the Milky Way and Andromeda by 3:1 ratio, for galaxies with $M_* > 10^7 M_\odot$. Digby et al. (2019) found that the star formation histories of dwarf galaxies can have significant variation

among galaxies, even if they have similar stellar mass and environment, and that on average the smallest ($10^5 < M_*/M_\odot < 10^6$) field dwarf galaxies formed the majority of their stellar populations at early times. These studies examined the overall effects of reionization on the dwarf population, but the details of which halo mass scales are directly affected by reionization, and whether a theoretical model can accurately describe this halo mass have not been studied in detail.

2.1.1 Gravity and Hydrodynamics solvers

The APOSTLE simulations were performed using a modified version of the P-GADGET3 code (Springel et al. 2008), developed for the EAGLE cosmological simulation (Crain et al. 2015; Schaye et al. 2015). This code uses particles to trace the otherwise continuous distribution of matter (dark matter and gas) in the Universe, with the mass-size of the particles varying as a function of resolution. All particles are affected by the force of gravity, which the code uses a hybrid scheme of Tree and Potential Mesh (TreePM) algorithms to solve for. In practice, this means that the force of gravity near the particle of interest is calculated via direct summation of the short range interactions, while the long range interactions are calculated by estimating the total gravitational potential on a mesh/grid system, and interpolating the force to the exact coordinates of the particle. This method combines the most important advantages of the tree algorithm, which has a natural scaling with high density regions, giving it an essentially unlimited dynamical range, and the significant computational efficiency of the Fourier-based mesh grid approach for long distance interactions. In order to avoid unphysical two-body scatterings between particles, gravitational interactions are also softened on small scales by representing each particle as a distributed mass with uniform density of physical size equivalent to the softening-length.

For modelling of the gas properties and pressure force, the P-GADGET3 code employs the Smoothed Particle Hydrodynamics (SPH) technique from Hopkins (2013). This is a Lagrangian method in which the properties of a continuous, inviscid, ideal gas can be described by its tracer gas particles. The fluids' continuous properties, such as density, temperature, and entropy, are calculated via a kernel-interpolation technique, which averages the properties of different particles over a given smoothing length. The Lagrangian method has the advantage over mesh-based methods (Eulerian) of naturally scaling the resolution in high density regions, as they traced by more particles. See Rosswog (2009); Springel (2010) for a more detailed review of the

SPH method in cosmological simulations.

2.2 APOSTLE parameters and Subgrid physics

The APOSTLE simulations adopted the WMAP-7 cosmological parameters (Komatsu et al. 2011), and were performed at three mass resolution (L1, L2, and L3), with particle mass of approximately 1.0×10^4, 1.2×10^5, and $1.5 \times 10^6 M_\odot$ for gas, and 5.0×10^4, 5.9×10^5, and $7.5 \times 10^6 M_\odot$ for dark matter. The gravitational softening lengths used were of 134, 307, and 711 pc, respectively. For the analysis in Chapter 4, we focus only on the high resolution runs, which were only performed for five of the twelve APOSTLE volumes.

As previously mentioned, there are a number of key physical processes that cannot be directly modelled in cosmological simulations, but are nonetheless essential for simulating the properties of galaxies. In this section, the subgrid prescriptions relevant for the onset and regulation of star formation in APOSTLE are described, namely, gas cooling and the UV-background, the interstellar medium and star formation (ie. the conversion of gas to stellar particles), and stellar feedback. The APOSTLE subgrid models use the same calibration as the EAGLE reference simulation, which were chosen to reproduce the observed galaxy stellar mass function at $z = 0.1$, and qualitatively reproduce the shape and size of galaxies (see Schaye et al. 2015; Crain et al. 2015, for the detailed methodology of the calibration process).

2.2.1 Radiative cooling, UV-background, and cosmic reionization

Gas can dissipate its internal energy via several cooling processes, including collisional excitation, recombination and free-free emission (Ferland et al. 1998). For APOSTLE, the radiative cooling and photoheating rates are calculated following the procedure outlined by Wiersma et al. (2009). The ionization state of the gas is calculated using the CLOUDY code (Ferland et al. 1998), assuming that the gas is dust-free, optically thin, and in ionization equilibrium with a photo-ionizing background. The gas is exposed to the time evolving, but spatially uniform, cosmic microwave and X-ray/UV-background from Haardt and Madau (2001).

The evolution of the background field is dependent on the parameterization of the reionization epoch in the simulation, which occurs at $z_{\rm reion} = 11.5$ in APOSTLE.

Before reionization, $z > 11.5$, the cosmic microwave background is modelled using the Haardt and Madau (2001) spectrum at $z = 9$, cropping energies above 1 Ryd. For $z < 11.5$, the full, time evolving, Haardt and Madau (2001) spectra is applied. To account for the fact that the gas is not optically thin prior to reionization, an extra 2 eV per proton mass are added, which ensures intergalactic gas is quickly ionized and heated to $\approx 10^4$K. For hydrogen, this is done at $z = 11.5$, while for helium the extra energy is distributed in redshift with a Gaussian centered at $z = 3.5$, of width 0.5.

2.2.2 Interstellar medium and star-formation

The APOSTLE simulations are not intended to resolve the multi-phase ISM or cold molecular gas complexes ($n_H > 10$ cm^{-3}, $T << 10^4$K). In order to prevent numerical instabilities on such small scales, the simulation imposes a minimum pressure floor on the gas, which takes the form of a "polytropic equation of state" (PEoS),

$$P_{\rm EoS} = P_0 \left(\frac{\rho_g}{\rho_0} \right)^{\Gamma}, \tag{2.1}$$

with $\Gamma = 4/3$ and where $P_0 = 1.1$ g cm^{-1} s^{-2} and $\rho_0/m_p = 0.1$ cm^{-3}. In practice, this forces high-density gas to have a temperature that simply reflects the effective pressure of the unresolved ISM, and cannot be trusted for other physical considerations, such as calculating neutral hydrogen fractions in post-processing.

Given the limitations of modelling cold molecular gas, star formation is only allowed to proceed at gas densities exceeding the threshold above which the cold molecular phase is expected to form. This is chosen to be 10 cm^{-3} for primordial gas but allowed to decrease with increasing metallicity, Z, in enriched gas regions (Schaye 2004);

$$n_{\rm thr}(Z) = \min \left[10^{-1}\ {\rm cm}^{-3} \left(\frac{Z}{0.002} \right)^{-0.64}, 10\ {\rm cm}^{-3} \right]. \tag{2.2}$$

For the systems we focus on in this paper, the fixed threshold is the more important of the two, since it is the one applicable to primordial/low metalicity gas.

Finally, because gas density in the early universe was very high, a simple density threshold would have allowed star formation at very high redshifts. For this reason, an overdensity requirement is also imposed, with gas density having to exceed 57.7 times the cosmic mean. However, the choice of overdensity requirement does not significantly affect the results (Schaye et al. 2015), largely due to the imposition of

the PEoS, which prevents gas from reaching high densities in low mass systems at high redshift.

2.2.3 Stellar Feedback

Stars, over the course of their lifetime, will deposit significant amounts of energy back into the inter-stellar-gas, via stellar winds, radiation, and supernovae. The feedback from particularly massive blue stars can suppress new star formation and its implementation in galaxy formation models is crucial for correctly reproducing the galaxy stellar mass function and galaxy morphology in simulations; insufficient stellar feedback has been shown to produce very compact disks (Crain et al. 2015).

In the APOSTLE simulation, stellar particles do not represent individual stars. Instead, they represent a population of stars which formed from the same molecular cloud, with the same age and metalicity. This is known as a simple stellar populations (SSPs), which has a Chabrier (2003) initial mass function (IMF) in the mass range 0.1-100$M_\odot$. The energy feedback released over a lifetime of the high-mass, blue, stars is implemented following Dalla Vecchia and Schaye (2012), where stellar particles will release their feedback energy in a stochastic manner to individual gas particles nearby. The energy given to each gas particle is fixed such that $\Delta T = 10^{7.5} K$, a value calibrated in Schaye et al. (2015), with the probability that any gas particle be heated proportionally to the total amount of energy released by the SSP. This energy corresponds to the release of 10^{51} erg per supernova, and assumes that all stars with masses 6-100 $M_\odot$ explode via this channel.

2.3 Halo finder

At any given snapshot, the simulation will simply output the location and velocity of the different tracer particles of dark matter, gas, and stars. These particles may have clumped into structures, such as halos and galaxies, with smaller bound objects in orbit (substructures). Identifying which particles belong to which substructures must be done algorithmically.

In APOSTLE, substructures are identified using the SUBFIND groupfinder (Springel et al. 2001; Dolag et al. 2009). Halos (structures) are first identified by running a friends-of-friends algorithm (FoF; Davis et al. 1985) on the dark matter particles, with a linking length 0.2 times the mean interparticle separation. Gas and stellar

particles are then assigned to the same FoF group as their nearest dark matter particle. SUBFIND, using all particles, then recovers gravitationally bound substructures within each FoF group, which we refer to as subhaloes. In this work we only study the properties of the main ("central") subhalo of each FoF halo, which usually sits at the bottom of the gravitational potential of the larger structure.

We use in our analysis all central halos found within a spherical volume with 3 cMpc radius, centered on the barycenter of the two main halos in each volume. The barycenter is calculated for each snapshot, spanning the redshift range from 0 to 20. We restrict our analysis to halos with $M_{200} > 10^7 M_\odot$, or the equivalent of about 200 dark matter particles. In practice, we shall see that no halos below $10^8\,M_\odot$ are able to form stars in these APOSTLE runs, so our analysis concerns mainly halos resolved with an equivalent of at least 2000 dark matter particles.

Chapter 3

The minimum halo mass for the onset of star formation

The effects of cosmological reionization on star formation in low mass halos have been theorized for quite some time (Ikeuchi 1986; Rees 1986; Efstathiou 1992). Under the presence of an external heating source, such as the cosmic UV background, gas is prevented from cooling in the shallow potential wells of lowest-mass halos, in turn preventing star formation (Couchman and Rees 1986; Chiba and Nath 1994; Quinn et al. 1996; Thoul and Weinberg 1996; Navarro and Steinmetz 1997; Bullock et al. 2000; Somerville 2002). From this early work, it is understood that the photo-ionizing background requires that halos exceed the atomic cooling limit by some factor in order to continue forming stars after reionization, potentially resolving the "Missing Satellites" problem in LCDM.

However, the exact value of this minimum mass is still under debate, as there have been a diverse set of arguments proposed to define it. For example, the earliest theoretical work used idealized Jeans mass arguments within the Press and Schechter (1974) formalism (eg. Couchman and Rees 1986; Rees 1986; Gnedin 2000; Benson et al. 2002) to find the *characteristic* mass scale below which the baryonic content of a halo is suppressed by half of the universal baryon fraction. This *characteristic* mass was later shown in Okamoto et al. (2008) to be significantly higher than that obtained using cosmological simulations. Even so, exactly how the characteristic mass should affect star formation is not clear. Star formation, which takes place at the bottom of the gravitational potential, should depend mainly on the properties of gas in that region, and only indirectly on the total baryonic fraction.

Benítez-Llambay and Frenk (2020) (henceforth BLF20) have recently re-cast the arguments for defining the minimum halo mass that can host star formation after reionization, considering the non-linear evolution of dark matter halos and the well described temperature-density relation of the inter-galactic-medium (IGM). Their work, which is described in more detail in the following section, assumes that, after reionization, gas in low-mass halos is in hydrostatic equilibrium with the dark matter potential, and in thermal equilibrium with the photo-ionizing background, which were shown to be good approximations in Benítez-Llambay et al. (2017).

3.1 Critical virial mass for star formation

We follow closely BLF20's model for the minimum virial mass needed for the onset of star formation in a halo.

After reionization, the photo-ionizing UV photons, together with gas cooling from collisional excitation of H and He line emission, lead to a tight link between gas density and temperature. This "equation of state" can be used, assuming hydrostatic equilibrium and a given shape for the dark matter gravitational potential, to infer the temperature profile of gas in halos of arbitrary mass. The resulting gas density profile can enable simple assessments regarding which systems can start forming stars, and when. The halo mass above which star formation can occur, which we term critical mass (M_{crit}), may be defined in function of some "threshold" reached by the properties of the gas inside the halo.

3.1.1 Temperature-density relation

The temperature-density ($T - \rho$) relation of photoionized gas in the IGM is well described by a single equation of state after reionization. This relation is characterized by two equilibrium regimes, as is shown in Fig. 3.1 at $z = 0$, taken from Benítez-Llambay et al. (2017). At low densities, the temperature rises steeply with increasing density, as a result of photoheating. This rise tracks the density at which the photoheating timescale equals the age of the Universe, shown by the green line. The temperature begins to turn down when the photoheating and radiative cooling timescales become comparable. At larger densities, the T-ρ curve drops from its maximum and approaches roughly 10^4 K, the minimum temperature needed to collisionally excite the Ly-α transition (see, e.g., Haehnelt et al. 1996; Theuns et al. 1998,

and references therein). The black dots in the plot show all the gas particles gravitationally bound to starless halos in a volume of the APOSTLE simulation, which track particularly well with the two equilibrium cooling curves.

In Fig 3.2, we show the $T-\rho$ relation for other redshifts (solid lines; $z < 11.5$), with data taken from Benítez-Llambay and Frenk (2020). Note that after reionization, the photoheating curve shifts towards lower densities, as the heating timescale increases. Additionally, the photoionizing background evolves in intensity over cosmic time, and in fact peaks around $z \sim 1$, after star formation in the universe also reached its peak at $z \sim 2$ (eg. Madau and Dickinson 2014). In this plot, we also include the polytropic equation of state (PEoS) imposed in the APOSTLE simulations, which results in the sharp upturn in temperature at high density (shown by dashed lines) (see section 2.2.2). This PEoS is implemented as a single pressure-density relation,

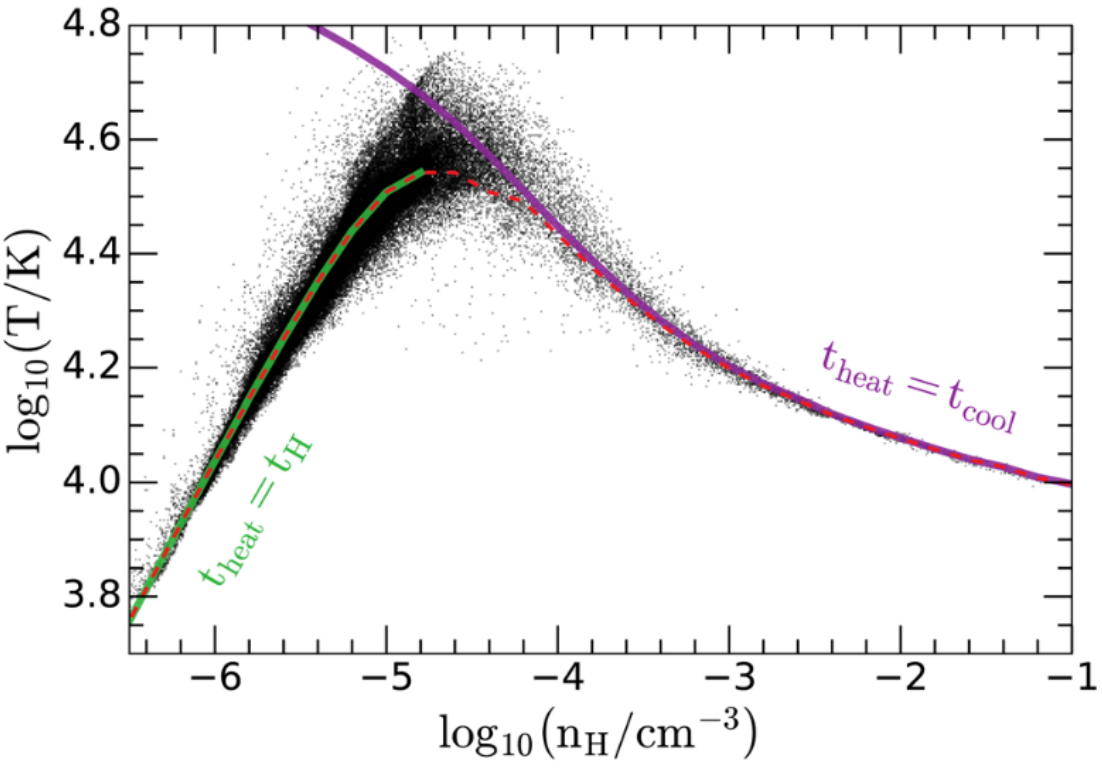

Figure 3.1: The temperature density of starless halos in the APOSTLE simulation. All bound gas particles to dark matter halos are shown as black dots. The green curve shows the loci where the photoheating timescale equals the age of the Universe, and the magenta line where photoheating and radiative cooling are in equilibrium. Taken from Benítez-Llambay et al. (2017).

but manifests itself as two different T-ρ relations, before and after $z_{\rm reion}$, because of the change in molecular weight that occurs at reionization. As we shall see below, the adoption of a PEoS curtails (artificially) the ability of low-mass halos to form stars before reionization.

Prior to reionization ($z > 11.5$), we assume the gas is isothermal at 10^4 K within the virial radius, for densities not affected by the PEoS. Recall that prior to reionization, gas in the IGM is mostly neutral with an expected discontinuity in the $T - \rho$ relation at the virial boundary, inside which gas has been heated by its own gravitational collapse. To highlight that the isothermal assumption does not apply outside the virial radius, the line shown in Fig. 3.2 is truncated at $n_H = 10^{-3}$ cm^{-3}. The assumption that gas exists at 10^4 K is also only valid for halos whose gravitational collapse can heat gas above that temperature, and therefore with virial mass with $T_{200} \geq 10^4$ K. Halos with virial temperature below $\sim 10^4$ K should have isothermal gas below $\sim 10^4$ K, which cannot excite Lyα line emission, and are therefore inefficient at cooling their gas (eg. Oh and Haiman 2002).

3.1.2 Structure of LCDM halos

In dark matter only simulations, the radial density profile of halos can be described with an NFW profile (Navarro et al. 1996b, 1997),

$$\rho(r) = \frac{\rho_0}{\frac{r}{R_s}\left(1 + \frac{r}{R_s}\right)^2} \tag{3.1}$$

which approaches a slope $\rho \propto r^{-1}$ in the region within the "scale" radius, R_s, and trends to $\rho \propto r^{-3}$ in the outer regions. When baryons are included, they can change the shape of the dark matter profile. In large systems, which have central regions dominated by baryons, the steepness of the dark matter halo in the inner regions is expected to increase (see, eg. Gnedin et al. 2004).

For dwarf galaxies, which are less efficient at converting their baryonic matter into stars than Milky Way sized galaxies, it could have been expected that their dark matter distributions followed closely with this dark matter only profile. This is generally not the case, as some dwarf galaxies are observed to lack dark matter in their central regions, when compared to the NFW profile (eg. Carignan and Freeman 1988; Moore et al. 1999b; Read et al. 2017). In particular, their dark matter profiles are flatter, $\rho \sim$ const., in the central regions, termed "cored" profiles.

The sudden removal of material from the inner galaxy, via, for example, a burst of star formation and subsequent ejection of a dense gas-disk, has been shown to affect the distribution of dark matter in the halo (Navarro et al. 1996a). This can result in cored dark matter profiles, which are observed in some (but not all) dwarf galaxies (eg. Oman et al. 2015). Later work suggested that with more plausible parameters for the initial system, a single powerful burst may not be sufficient to generate a cored profile (Gnedin and Zhao 2002; Read and Gilmore 2005), but a less violent and repeating mechanism could (Pontzen and Governato 2012; Governato et al. 2010).

At sufficiently low masses however, star formation efficiency is low enough that dwarf galaxies are expected to have a dark matter profile that follows the "cuspy" NFW profile (Di Cintio et al. 2014; Tollet et al. 2016). However, the dark matter

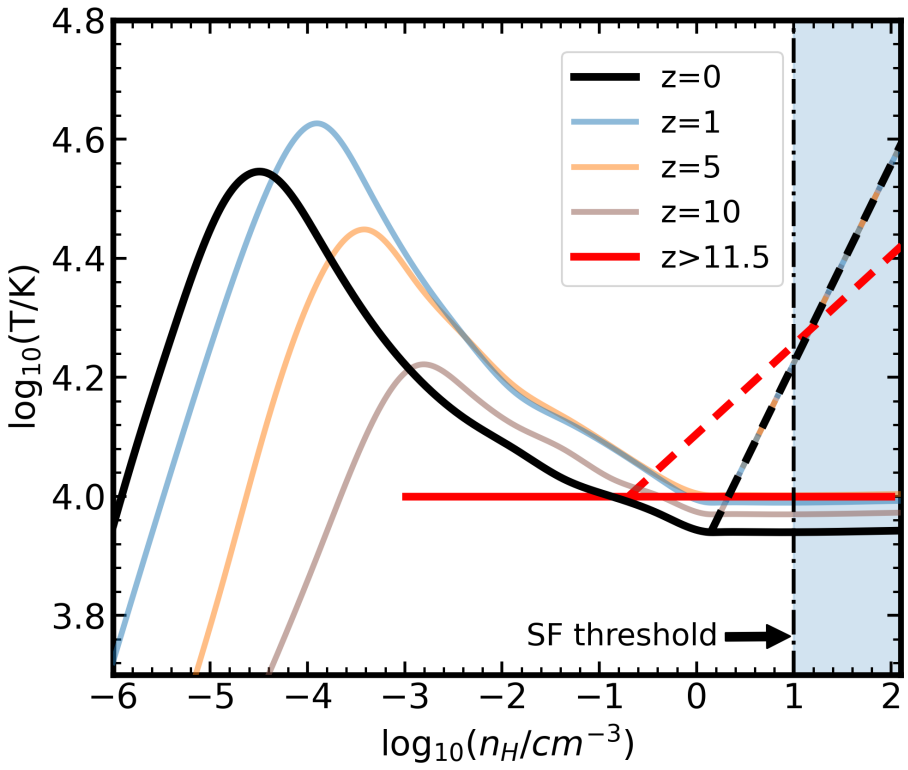

Figure 3.2: Gas temperature-density relation assumed in our modeling at different redshifts. At high densities, dashed lines indicate the polytropic equation of state (PEoS) adopted in the APOSTLE/EAGLE simulations. In that regime, solid lines assume that the gas is isothermal. Prior to reionization, our model assumes that, at low densities, the gas inside the virial radius of critical halos is isothermal at 10^4 K (thick red line). Densities above the APOSTLE star formation threshold ($n_H = 10\,\mathrm{cm}^{-3}$) are highlighted in light blue.

profiles of these systems have not been measured yet, since they have few stars and no gas with which to measure a rotation curve. To illustrate the stellar mass range in which the core - cusp transition is expected to occur, Fig. 3.3 shows the dark matter profiles of three dwarfs galaxies simulated using the FIRE-2 code (Fitts et al. 2017). The profile of the lowest mass dwarf galaxy (left panel) is identical, whether baryons are included (HYDRO) or whether it is a dark matter only run (DMO). On the other hand, the brighter dwarfs show a flattening of the dark matter profile when baryons are included compared to the dark matter only run, particularly for the higher mass, $M_* = 10^7 M_\odot$, galaxy.

3.1.3 Hydrostatic Equilibrium model

The equation of hydrostatic equilibrium,

$$\frac{1}{\rho}\frac{dP}{dr} = -\frac{GM(r)}{r^2} \tag{3.2}$$

can be combined with the equation for ideal gas, and re-written in terms of dimensionless variables,

$$\left(\frac{\tilde{T}}{\tilde{\rho}} + \frac{d\tilde{T}}{d\tilde{\rho}}\right)\frac{d\tilde{\rho}}{d\tilde{r}} = -2\frac{\tilde{M}(\tilde{r})}{\tilde{r}^2}, \tag{3.3}$$

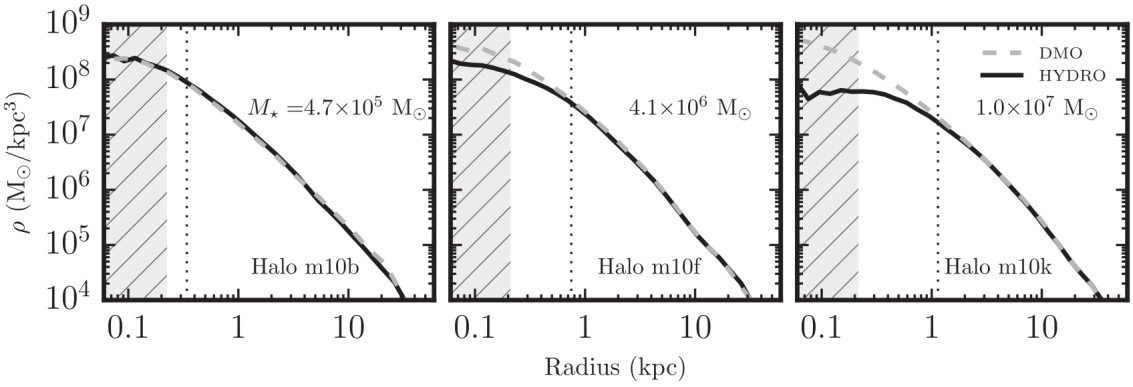

Figure 3.3: Comparison of dark matter radial density profiles using baryon only simulation (HYDRO) or dark matter only runs (DMO). Taken from Fitts et al. (2017)

where $\tilde{\rho} = \rho/\bar{\rho}_{\rm bar}$, $\tilde{T} = T/T_{200}$, $\tilde{M} = M/M_{200}$, $\tilde{r} = r/r_{200}$, and $\bar{\rho}_{\rm bar} = \rho_{\rm crit}\Omega_{\rm bar}$[1]. Here the halo virial temperature is defined as $T_{200} = (\mu m_p/2k_B)V_{200}^2$, where μ, m_p and k_B are the mean molecular weight[2], the proton mass, and Boltzmann's constant, respectively. V_{200} is the halo circular velocity at r_{200}, defined by $V_{200}^2 = GM_{200}/r_{200}$.

In practice, to solve for the spatial density of gas, we begin by writing the LHS and RHS of eq. 3.3 in integral form,

$$F(\tilde{\rho}) = \int_{\tilde{\rho}_n}^{\tilde{\rho}} \left(\frac{\tilde{T}}{\tilde{\rho}'} + \frac{d\tilde{T}}{d\tilde{\rho}'}\right)\Bigg|_{\tilde{\rho}'} d\tilde{\rho}' \tag{3.4}$$

$$G(\tilde{r}) = -2\int_{\tilde{r}_n}^{\tilde{r}} \frac{\tilde{M}(\tilde{r}')}{\tilde{r}'^2} d\tilde{r}' \tag{3.5}$$

and from which the gas density is obtained numerically, by inverting F:

$$\rho(\tilde{r}) = F^{-1}[G(\tilde{r})]. \tag{3.6}$$

In order to solve Eq. 3.5, we assume that the dark matter potential is dominant over the baryonic matter, and for simplicity, that dark matter halos are spherically symmetric and well approximated by NFW profiles (Navarro et al. 1996b). The validity of these assumptions has been tested by Benítez-Llambay et al. (2017); Benítez-Llambay and Fumagalli (2021) using cosmological hydrodynamical simulations. The total enclosed mass profile can then be written as,

$$\tilde{M}(\tilde{r}) = \frac{\ln(1+c\tilde{r}) - c\tilde{r}/(1+c\tilde{r})}{\ln(1+c) - c/(1+c)}, \tag{3.7}$$

where the c is the concentration parameter, $c = r_{200}/r_s$. BLF20 assumes a constant concentration of $c = 10$ when modelling their critical mass. We choose to model the concentration, $c(M_{200}, z)$, as a function of mass and redshift with the parameterization proposed by Ludlow et al. (2016), valid for the WMAP-7 LCDM cosmology.

To solve Eq. 3.4 we require the temperature-density (T-ρ) relation for the intergalactic gas, described in the previous section 3.1.1, as well as a boundary condition for the gas density. For the boundary condition, we assume two different behaviours

[1] $\Omega_{\rm bar}$ is the average density of baryonic matter as a fraction of the critical density, $\rho_{\rm crit}$, needed for a flat Universe. $\rho_{\rm crit}$ is defined as $3H^2/8\pi G$. In WMAP7, $\Omega_{\rm bar} = 0.0455$ and $H_0 = 70.4$km s^{-1} Mpc^{-1} (Komatsu et al. 2011)

[2] Unless otherwise noted, we assume a constant $\mu = 0.6$, as appropriate for a fully ionized gas of primordial composition.

prior to and after reionization. After reionization, we assume that the density of gas at infinity ($r \to \infty$) is equal to the average baryonic density of the Universe ($\bar{\rho}_{\rm bar}$), similar to BLF20.

Prior to reionization, the $T - \rho$ relation for the inter-galactic medium is not well constrained, and therefore the relation described in section 3.1.1 is not applicable beyond the virial radius. To circumvent this, the boundary condition is defined at the virial radius, such that the total enclosed gas-mass within r_{200} equals the universal baryon fraction (i.e., $M_{gas}(r < r_{200}) = f_{\rm bar} M_{200}$).

3.1.4 Analytic gas density profiles

Using Eq. 3.6 we may now compute the gas density profile of a halo with gas in hydrostatic equilibrium at any redshift, using the appropriate T-ρ relation, as shown in Fig. 3.2. The population of dark matter halos which are expected to have gas in hydrostatic equilibrium are primarily "dark" halos - ie. those that have not formed any stars - which were coined in BL17 as RELHICs, for REionization Limited HI Clouds.

We illustrate this point in Fig. 3.4, where we apply our hydrostatic equilibrium model to an example halo from the APOSTLE simulation at $z = 0$, with virial mass $M_{200} = 10^{9.65} M_\odot$. The dashed curve in the top panel shows the total gravitational acceleration profile, $a(r) = GM(r)/r^2$, of the dark matter particles in the halo, and the dots in the bottom panel indicate the gas profile of this RELHIC. The NFW profiles of three halos with the same virial mass, but different concentrations ($c = 5$, 10, and 15), are also shown with thick colored lines. For the appropriate concentration ($c \approx 10$), the gas profile computed by solving Eq. 3.6 matches the density profile of the simulation data remarkably well[3].

The shaded region in the bottom panel of Fig. 3.4 highlights the densities above the star formation threshold assumed for primordial gas in APOSTLE. At a fixed halo mass, the resulting density profile is highly dependent on halo concentration. For example, for the halos with concentration $c = 5$ and 10 the gas in the halo would remain in hydrostatic equilibrium without forming stars, whereas for $c = 15$, it would begin forming stars at its centre. This illustrates that not only halo mass, but also concentration, determine which halos will host luminous galaxies and which

[3]In order to best fit the data of this example RELHIC, we set a boundary condition equal to the RELHIC gas density at $r = r_{200}$, instead of the condition at infinity which we use in the critical mass modeling at this redshift

will remain "dark".

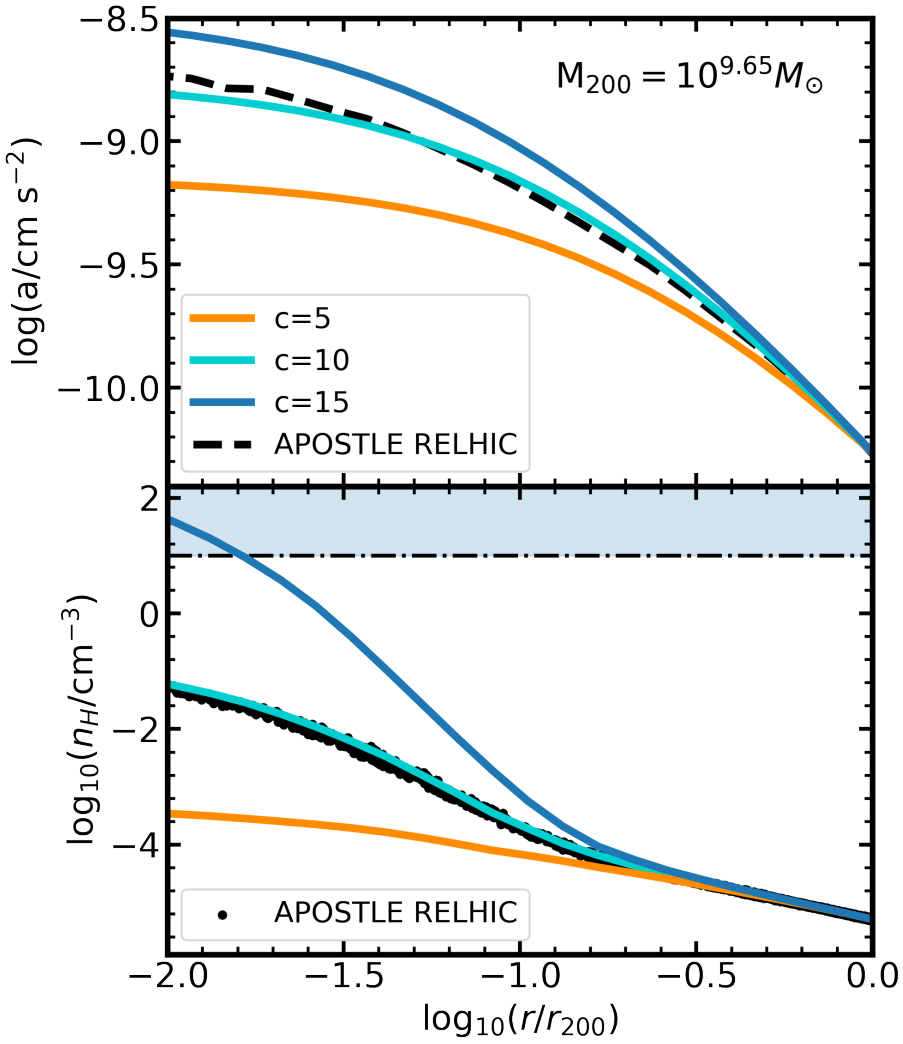

Figure 3.4: *Top:* Acceleration profile ($a(r) = GM(r)/r^2$) of $M_{200} = 10^{9.65} M_\odot$ NFW halos of different concentration at $z = 0$ (solid colored lines). The dashed black curve is the acceleration profile of an APOSTLE RELHIC of the same virial mass. *Bottom:* Gas density profile of the RELHIC (black dots) as well as model density profiles computed assuming hydrostatic equilibrium (Eq. 3.3; solid colored lines). Densities above the APOSTLE star formation threshold are highlighted in blue.

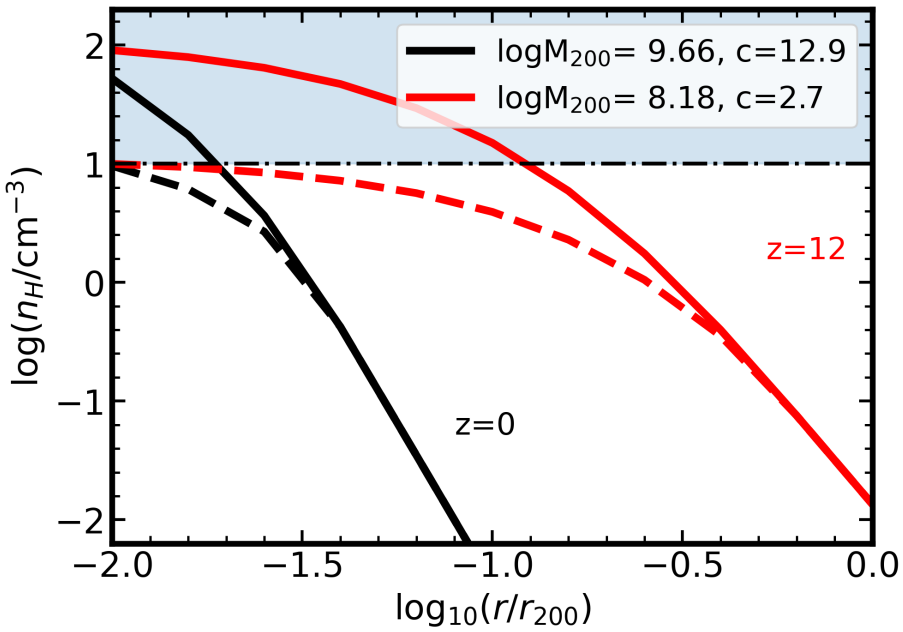

Figure 3.5: Model gas density profiles assuming that the gas remains isothermal at high densities (solid curves) or that it follows the APOSTLE/EAGLE polytropic equation of state (PEoS; dashed curves). Two NFW halos are shown, at $z = 0$ and at $z = 12$, with masses and concentrations as listed in the legend. Densities above the APOSTLE star formation threshold are highlighted in blue.

We examine next the role of the PEoS imposed on high-density gas in APOSTLE. Fig. 3.5 shows the gas density profiles of two NFW halos at two different redshifts, with virial masses selected such that their central density corresponds to the star formation threshold $n_H = 10\text{cm}^{-3}$ when computed including the PEoS (dashed lines). The gas density profile if the PEoS is not included, for the same halos, is shown as solid line. Concentrations for each halo are computed from the average concentration expected from the Ludlow et al. (2016) mass-concentration-redshift relation. The adoption of a PEoS clearly depresses the central gas densities. This is true in particular prior to reionization where the PEoS renders most halos below $\sim 10^8\,M_\odot$ (artificially) ineligible for star formation. However, because of the lower NFW concentration and the increased density of matter in the universe at high redshift, the imposition of the PEoS also affects the gas density in the halo within a larger volume. As we shall see below, all APOSTLE halos that begin forming stars at $z > z_{\rm reion}$ exceed a virial mass of $\sim 10^8\,M_\odot$, which is likely an artificial result of the imposed PEoS.

3.1.5 Halo concentration and central gas density

To isolate the effects of concentration on the gas profile, we adopt the T-ρ relation without a PEoS in this section. In Fig. 3.6 we summarise the effects of concentration on gas properties. The top panel shows, as a function of halo mass at $z = 0$, the impact on the central gas density (defined as n_c, or the density at $r = 0.01\, r_{200}$) of varying the average halo concentration about the value, $c \approx 13$, expected for LCDM (Ludlow et al. 2016). Average-concentration halos (solid black curve) are expected to become eligible for star formation for virial masses exceeding $10^{9.63} M_\odot$, but this boundary varies somewhat for lower or higher-than-average concentration halos.

The variation in terms of "critical" mass, however, is not large, only about a factor of ~ 2 for concentrations between 5 and 20. We conclude that, although halo concentration plays a role in determining which halos are expected to remain "dark" or to host luminous systems, it appears to be secondary compared with the role of halo mass.

Indeed, this is shown in the bottom panel of Fig. 3.6, which is analogous to the top, but plots the total gas mass expected within the virial radius, and how it varies with halo concentration. For average-concentration halos (solid black curve) the total gas mass is seen to match the expected total baryonic content of the halo at $M_{200} \sim 10^{9.65} M_\odot$ and to diverge rapidly at higher masses: gas in such halos is unable to stay in hydrostatic equilibrium and would collapse to the centre and trigger the onset of star formation. This is the rationale for the "critical mass" for star formation advocated by BLF20.

Comparing the top and bottom panels of Fig. 3.6 shows that defining the "critical mass" either by total gas content or central gas density gives similar results (within a factor of ~ 2; note that none of these curves include the effects of the EAGLE PEoS). This provides further evidence for the robustness of the concept of critical mass. In addition, it explains the good agreement reported by BL21 between the BLF20 critical mass (derived using total gas mass) and the results of cosmological simulations using the EAGLE code, where star formation is triggered once gas density goes above a minimum threshold value.

Finally, we explore in Fig. 3.7 how the central gas density varies as a function of redshift for halos of fixed mass, as labeled. Solid curves use the T-ρ relations of Fig. 3.2, while the dashed curves correspond to models that include the PEoS modification at high gas densities, implemented in the APOSTLE simulation. Each of these

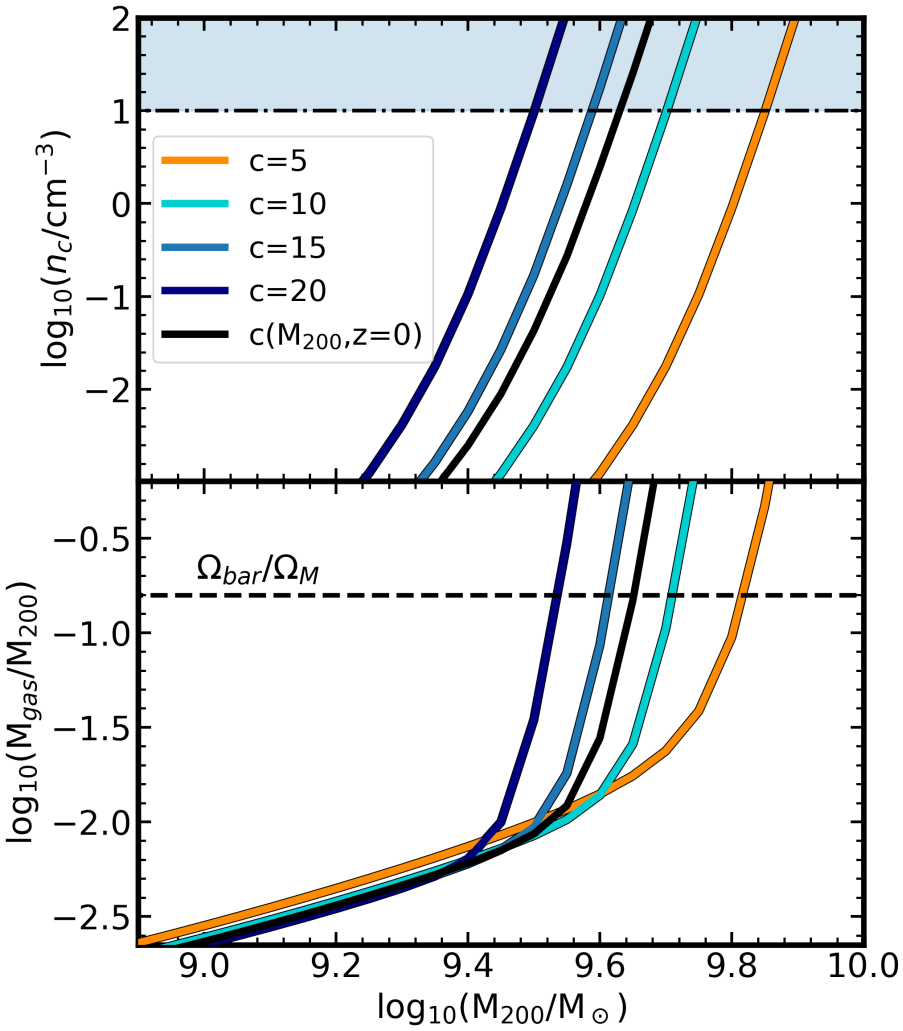

Figure 3.6: *Top:* Central gas densities, n_c (defined as n_H at $r = 0.01\, r_{200}$), calculated assuming hydrostatic equilibrium and the T-ρ relation without PEoS (solid curves in Fig. 3.2). Four NFW profiles with different concentrations are shown, including one (shown in black) that follows the average concentration of LCDM halos, which in this mass range is $c \sim 13$ (Ludlow et al. 2016). *Bottom:* Total gas mass within the virial radius for halos shown in the top panel.

curves assumes the concentration-mass-redshift dependence of Ludlow et al. (2016). For curves of the same mass, the epoch of reionization constitutes a discontinuity in the curves which is caused by the changing boundary condition and $T - \rho$ relation across this redshift. The intersection of each curve with the central density threshold of $n_c = 10\mathrm{cm}^{-3}$ corresponds to the redshift at which that mass equals the "critical" mass in APOSTLE, and halos above this mass can host star formation. The critical

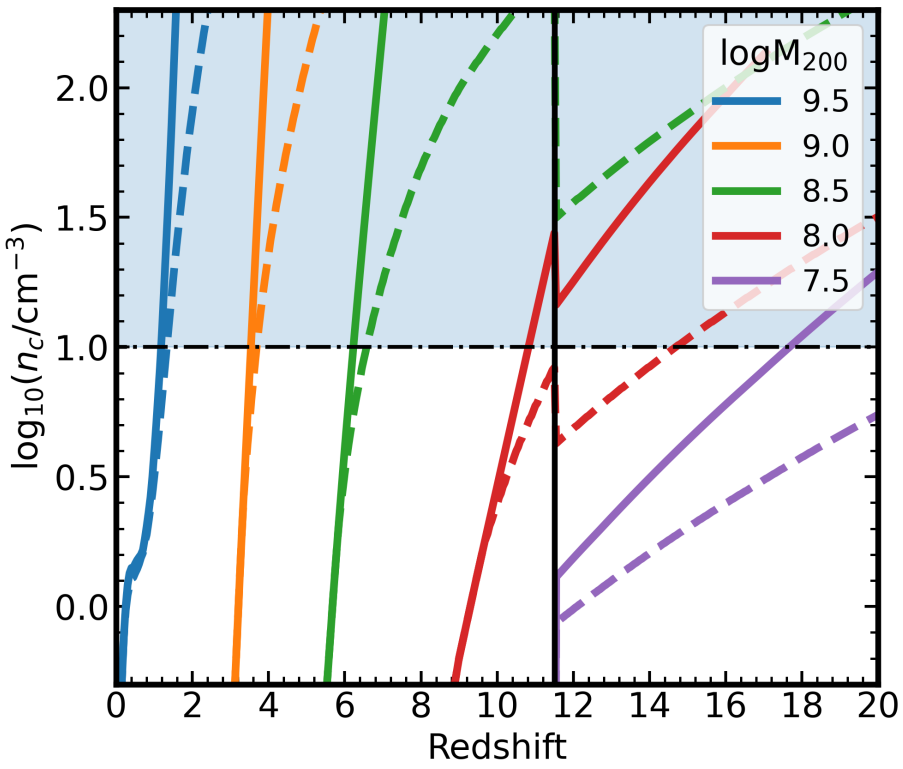

Figure 3.7: Central gas densities, n_c, computed assuming hydrostatic equilibrium and that the gas is isothermal at high densities (solid curves) or that it follows the APOSTLE/EAGLE PEoS (dashed curves). Each curve corresponds to halos of different virial mass, as listed in the legend. Each of these halos becomes "critical" at the redshift where they cross the star formation threshold. The reionization redshift is shown by the black vertical line. Densities above the star formation threshold of APOSTLE are highlighted by the shaded blue region.

mass clearly decreases systematically with redshift, driven primarily by the increase in gas density and the evolution of the T-ρ relation. The critical mass is also sensitive to the PEoS assumption, particularly at high redshifts where the difference between the two sets of lines grows.

3.1.6 Definition of Critical Mass

Once the gas density profile is known, a criterion for the onset of star formation needs to be specified, which in turn sets the minimum value of the halo mass needed for star formation to begin. After reionization, BLF20 adopted a criterion based on the total gas content within the virial boundary of a halo, obtained by integrating

$\rho_{\rm gas}(r)$. Above a redshift-dependent minimum mass, $M_{\rm crit}(z)$, the gas content exceeds $f_{\rm bar}\, M_{200}$, the total baryonic mass expected within r_{200} according to the universal baryon fraction, $f_{\rm bar} = \Omega_{\rm bar}/\Omega_{\rm M}$. The theoretical total gas mass quickly diverges for masses greater than $M_{\rm crit}$, indicating that pressure alone cannot stop gas from flowing to the centre of a halo, where it should turn into stars.

A different criterion is adopted for the APOSTLE simulation, based instead on the central (maximum) density of the gas. This criterion is better suited to the choices made in cosmological hydrodynamical simulations, which often rely on a minimum "threshold" gas density for star formation to proceed. Although different, the two criteria actually give similar results for $M_{\rm crit}(z)$, as will be discussed in Sec. 3.1.7.

Prior to reionization, the APOSTLE fiducial and BLF20 critical mass models differ substantially. BLF20 replace the hydrostatic equilibrium assumption, and instead model the critical mass as the halo mass needed for atomic cooling. The reasoning for this change is justified by the timescale constraint in which gas can cool sufficiently to form stars, before the photo-ionizing background heats the gas in IGM. In order to dissipate the thermal energy gained from the gravitational collapse of gas into the halo, the halo needs to be massive enough to allow for gas to heat up to $\sim 10^4$ K. This is the lowest temperature which can excite atomic line emission. In practice, the BLF20 requires that the virial temperature of the halo be higher than $T_{200} = 7\times10^3$ K to define the critical mass.

For the APOSTLE fiducial model proposed here, we attempt to extend the hydrostatic equilibrium formalism, in an attempt to preserve the critical mass definition based on the central density "threshold" of the APOSTLE simulation, but also crucially to include the effects that the PEoS has on the critical mass value. However, recall from section 3.1.3, that the boundary condition is discontinuous at reionization. Prior to reionization, we set the boundary condition such that the total enclosed gas mass within $r200$ corresponds to the universal baryon fraction, instead of using a fixed value at $r \to \infty$.

3.1.7 Critical mass model comparison: BLF20 vs APOSTLE

We are now ready to compute a critical mass as a function of redshift that can be compared directly with the results of the APOSTLE simulation. We shall refer to this as the APOSTLE fiducial model, and it is shown by the black dashed curve in Fig. 3.8, which traces the halo mass that hosts a system with $n_c = 10$ cm^{-3}, the APOSTLE

primordial gas threshold for star formation. The black dashed curve assumes average concentrations from the Ludlow et al. (2016) $c(M, z)$ relation, and the T-ρ relations (including the effects of EAGLE's PEoS) shown in Fig. 3.2.

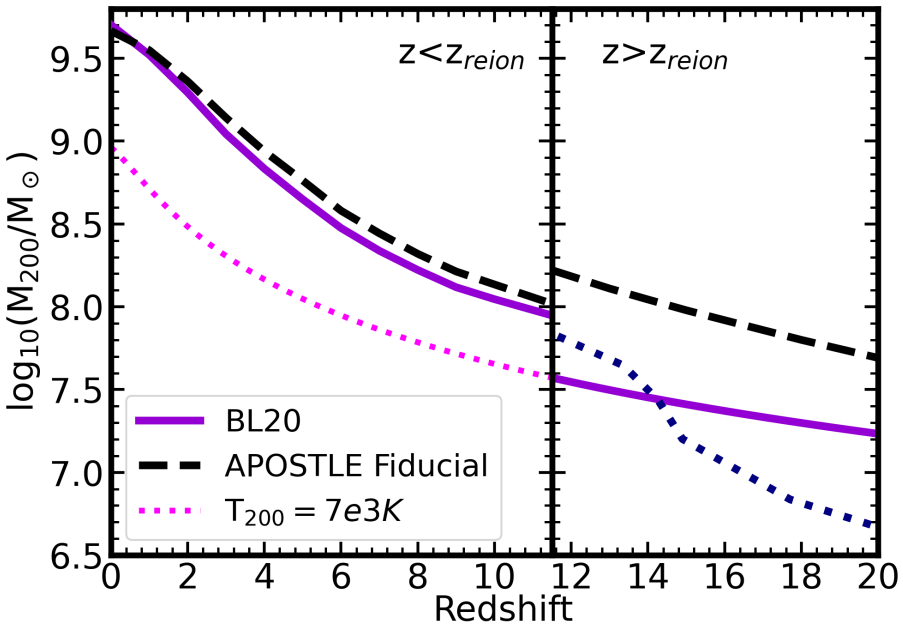

Figure 3.8: Critical mass curves as a function of redshift: solid purple curve uses the Benítez-Llambay and Frenk (2020) definition. Our fiducial APOSTLE model is shown in dashed-black, calculated with the T-ρ relations shown in Fig. 3.2, including the PEoS. For reference, the magenta dotted line show the virial mass for a fixed $T_{200} = 7000$ K, whereas the blue dotted line tracks, prior to reionization, the H_2-cooling critical mass from Tegmark et al. (1997).

We compare our APOSTLE fiducial model with the critical mass curve from BLF20, shown by the thick magenta curve in Fig. 3.8. This curve is computed using the total gas mass criterion illustrated in the bottom panel of Fig. 3.6. The BLF20 model adopts, for simplicity, a constant concentration of $c = 10$, and that the critical mass is approximated by the atomic cooling mass, with $T_{200} = 7 \times 10^3$ K, prior to reionization.

The most notable change between the black and magenta lines is that the jump to lower $M_{\rm crit}$ at $z > z_{\rm reion}$ expected from BLF20 is affected when introducing the PEoS. The PEoS reduces substantially the central gas densities that the gas may reach in halos near the critical boundary before reionization. Because of this, we expect only APOSTLE halos that exceed $10^{7.7}$-$10^{8.2}\,M_\odot$ to be able to start forming stars before reionization in our APOSTLE runs. Note that this is higher than either the critical

boundary expected either from the H-cooling limit (set at 7000 K; magenta curve) or from H_2-cooling, indicated by the blue dotted line (Tegmark et al. 1997). H_2-cooling is the mechanism through which primordial gas is expected to cool to form the first stars (Pop III). However, it should not be a dominant cooling mechanism for the formation of Pop II stars, because any H_2 would have been readily dissociated via the Lyman-Werner radiation of the first stars (eg. Skinner and Wise 2020; Kulkarni et al. 2021). It is simply included in this plot for reference.

Chapter 4

Comparison to APOSTLE data

4.1 The onset of star formation

We begin by analysing how well the critical mass model presented in the previous section describes the onset of star formation in the APOSTLE simulation. This is shown in Fig. 4.1, where we plot the virial mass of a halo at the time it forms its first star. Individual systems are shown with squares, colored by their concentration, computed from the ratio between maximum circular velocity, $V_{\rm max}$, and V_{200}, assuming NFW profiles. The critical mass curves from BLF20 (solid magenta) and from our APOSTLE fiducial model (black) are also shown.

Despite the simplicity of the critical mass model, it appears to capture well the main trends highlighted in Figure 4.1. In particular, it is clear that the minimum mass needed to ignite star formation increases steadily with decreasing redshift, and that the boundary is well approximated by the dashed black line. There seems to be no jump in the mass needed to start forming stars at reionization (as predicted by the BLF20 model), but rather a fairly well-defined minimum of order $10^8\,M_\odot$ in APOSTLE. As discussed in section 3.1.7, this is expected from the introduction of a polytropic equation of state (PEoS) in APOSTLE. Indeed, the black curve model, which includes the PEoS, is in much better agreement with the simulation data prior to reionization. We therefore expect that APOSTLE systematically underestimates the redshift at which early-collapsing halos may start forming stars before reionization, and possibly also the total number of luminous systems formed.

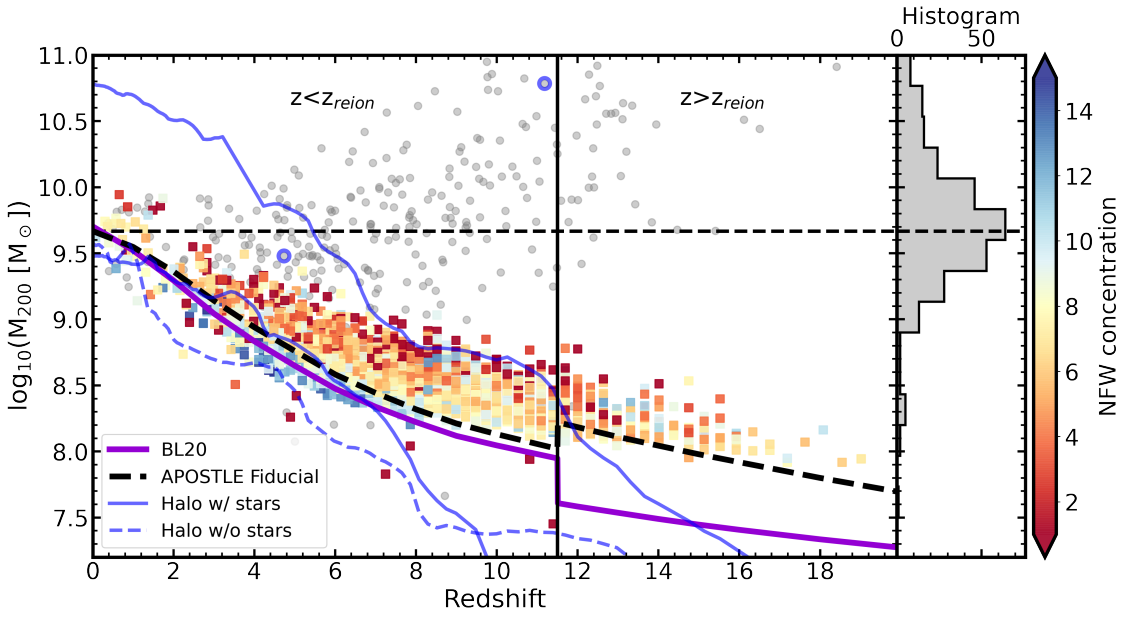

Figure 4.1: Squared symbols show the virial mass of APOSTLE halos at the time when their first star is formed, colored by concentration. The magenta curve is the BLF20 critical mass; the dashed black curve is the APOSTLE fiducial model from Fig. 3.8. Grey circles indicate the redshift of formation of the oldest star as a function of virial mass for APOSTLE centrals with $M_{200} < 10^{11}\,M_\odot$ at $z = 0$. The blue lines show three example halo mass assembly histories. Two of the halos host luminous galaxies at $z = 0$ (solid blue); the other hosts a star-less RELHIC (dashed blue). The time at which the two luminous halos began star forming are highlighted by a blue-circle. The histogram in the right panel shows the distribution of M_{200} for the grey data points, with a clear peak near the critical mass at $z = 0$.

4.1.1 NFW concentration and scatter of virial masses

A few other points are worth noting in Fig. 4.1. One is that, at fixed redshift, the scatter in halo mass at the time of first star formation correlates clearly with halo concentration: the higher the concentration, the lower the mass needed to trigger star formation, as expected from our discussion of Fig. 3.4. However, the scatter of virial masses at a fixed redshift cannot be fully explained by the variation of NFW concentrations in our critical mass model. This is shown in Fig. 4.2, where the NFW concentration at the onset of star formation in now averaged over a hex-bin area, to highlight the overall trend with concentration. Four critical-mass lines, calculated using the same definition as the APOSTLE fiducial model, but assuming fixed concentrations, $c = 15$, 10, 5, and 2, are also shown. The APOSTLE fiducial

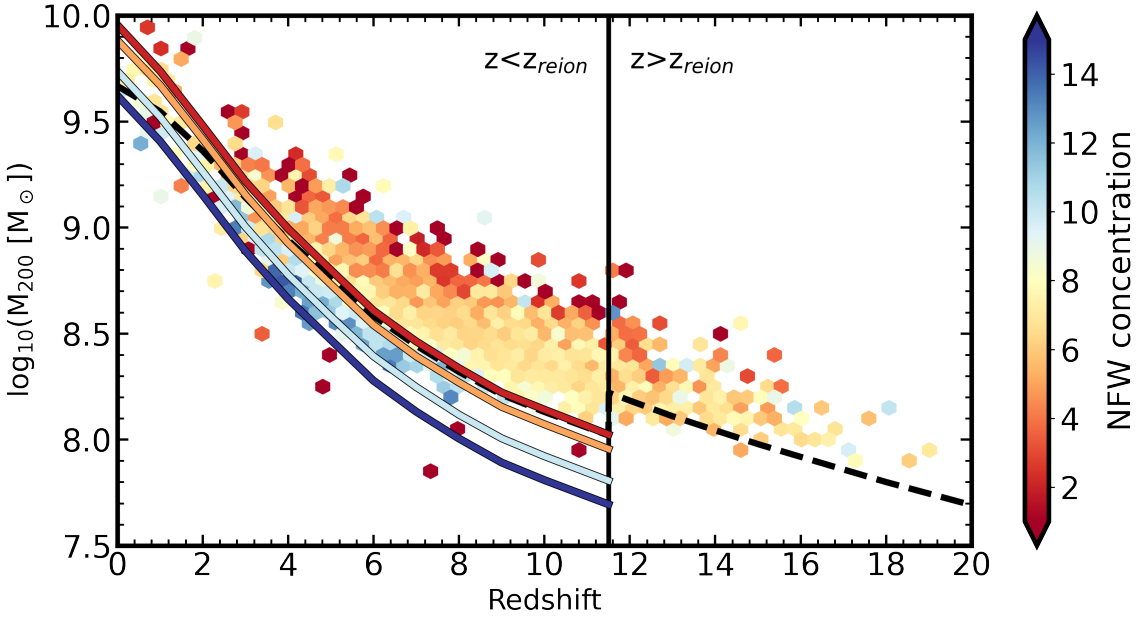

Figure 4.2: Hex-bin plot showing the averaged NFW concentration in a given virial mass and redshift bin. Four critical-mass lines are shown using the same definition as the APOSTLE fiducial model, except that they are calculated using fixed NFW concentration, c=15 (navy blue), c=10 (turquoise), c=5 (orange), and c=2 (red).

model (dashed-back) is calculated with the mass and redshift dependent Ludlow et al. (2016) concentration relation, which varies from $c \sim 3$ for $M_{200} \sim 10^8 M_\odot$ at $z = 11.5$ to $c \sim 13$ for $M_{200} \sim 10^{9.7} M_\odot$ at $z = 0$. The intersections of the APOSTLE fiducial model with the different constant concentration lines correspond to the loci where the concentration of the Ludlow et al. (2016) relation is the same as the fixed concentration line.

The variation in virial masses predicted between the $c = 15$ and $c = 2$ lines, which span the same range of concentrations as the APOSTLE data, do not cover the same range of virial masses at any given redshift as the APOSTLE data. For example, at $z \sim 4$, where the highest concentration line $c = 15$ matches well with the highest concentration halos forming stars in APOSTLE, there are halos forming stars at $M_{200} \sim 10^{9.4} M_\odot$, which is 0.4 dex higher than that predicted by the lowest concentration critical mass line, $c = 2$. Extending this analysis to other redshifts, it appears that the higher concentration APOSTLE halos are better described by the corresponding fixed concentration critical mass model, than the low concentration halos. In other words, the blue lines describe the virial mass at the onset of star

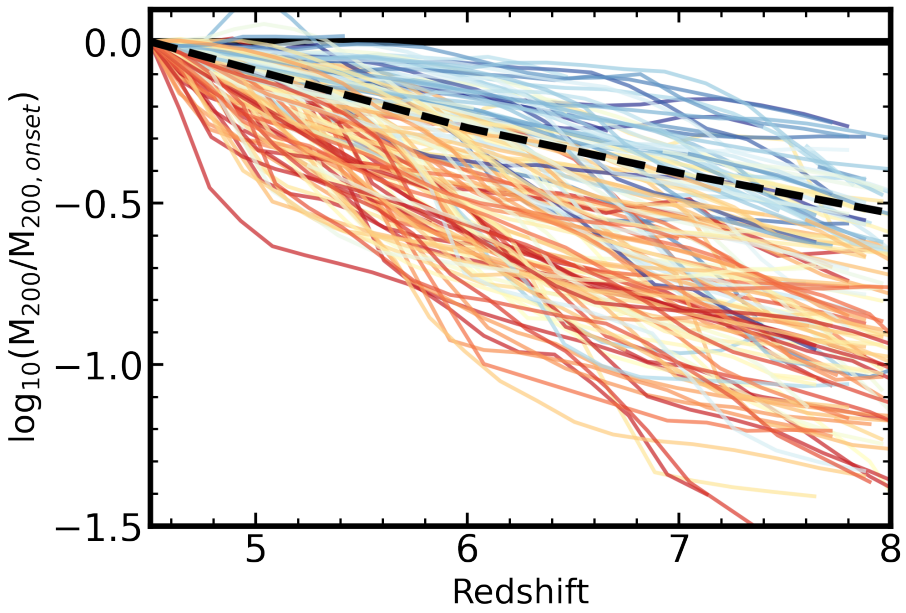

Figure 4.3: Normalized mass-assembly-history of all halos which begin forming stars between $4 < z < 5$, colored by NFW concentration at the onset of star formation. Evolution of the APOSTLE critical mass is shown in the black-dashed line.

formation for blue (high-concentration) halos, while the low concentration halos (red) are always above the expected critical mass line for their concentration (red line).

A full solution to this problem is not explored in this work. However, a possible explanation for the excess virial mass of the low concentration halos is hinted at in the halo mass assembly histories. Fig.4.3 shows the mass assembly history of all halos which form their first star between $4 < z < 5$, normalized by their virial mass at that moment, and colored by their NFW concentration. The lowest concentration halos, on average, grow faster than the APOSTLE critical mass (black-dashed) in this redshift range, in contrast with the high concentration halos, which grow nearly parallel to the critical mass line. If there exists some time interval between a halo exceeding the critical mass value and the onset of star formation, such a "delay time" would allow all halos to continue growing after they first exceed the critical mass value. The difference in mass assembly histories as a function of NFW concentration would cause low concentration halos to grow more than the critical mass before forming stars, while high concentration halos grow by same amount as the the critical mass and would therefore have a virial mass at the time of star formation similar to the critical mass. Proving that such a "delay time" mechanism exists would significantly improve our understanding of low-concentration halos and the critical mass model

presented.

In Fig. 4.2, there are a few hex-bins which show some halos begin forming stars below critical while also having low concentration, opposite to the trend just discussed. This population is revisited in more detail in section 4.3.

4.1.2 When does star formation begin?

A robust result to glean from Fig. 4.1 is that very few systems form their first stars after $z \sim 2$ or so. We show this in detail in Fig. 4.4, where the grey histogram corresponds to the distribution of ages of the oldest star in all APOSTLE luminous systems with present-day virial masses $M_{200} < 10^{11}\, M_\odot$. Indeed, only 16 out of 279 field dwarfs at present day started forming stars after $z = 2$ (10 Gyr lookback time), and no new galaxy has formed in the most recent 4 Gyrs. This trace population corresponds to dwarfs with uncommon mass accretion histories, which first reached the critical mass fairly recently. Such population has been more thoroughly analyzed by Benítez-Llambay and Fumagalli (2021). On the other hand, the great majority of $z = 0$ luminous systems date to lookback times at least as old as 12 Gyrs, which is in line with observations that indicate that all dwarf galaxies in the Local Group host some ancient stellar population (eg. Weisz et al. 2014a; Brown et al. 2014).

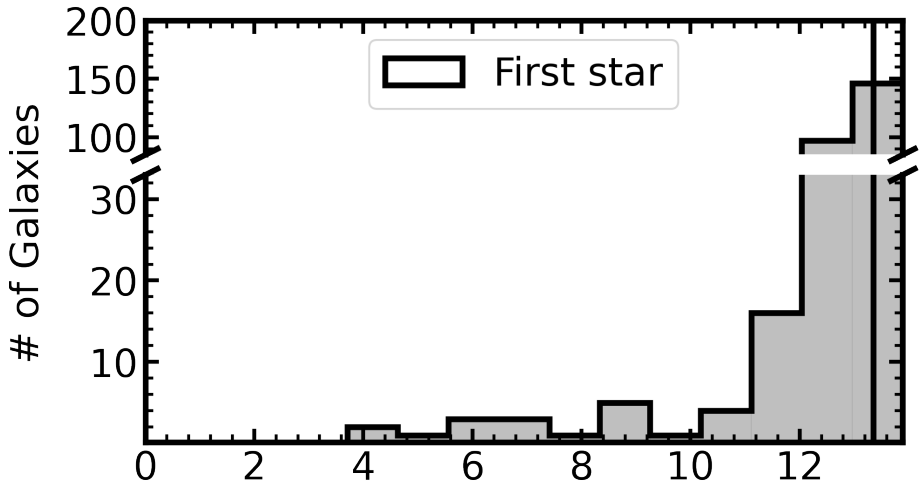

Figure 4.4: Age distribution of the oldest star particles in APOSTLE field dwarfs identified at $z = 0$ (grey data points in Fig. 4.1).

It is also clear from the grey circles in Fig. 4.1, which show the virial mass of central field dwarfs at $z = 0$, that more massive systems started forming their first

stars before smaller halos. However, it is very difficult to discern the difference in stellar age in these very old populations (the lookback time between $z = 2$ and $z = 11$ only changes from 10.4 to 13.3 Gyrs), so this halo mass gradient would be very difficult to confirm observationally.

The great majority of luminous dwarfs in APOSTLE start forming stars early on (lookback time > 10 Gyr). The reason for this may be attributed to the mass growth history of halos with masses close to the critical mass of $\sim 10^{9.7} M_\odot$ at present day. We show three such mass accretion histories (i.e., the redshift evolution of the mass of the most massive progenitor of a system identified at $z = 0$) with blue curves in Fig. 4.1. Two of these, shown in solid blue, correspond to halos hosting luminous dwarfs at present, and they start forming stars roughly at the time (identified by open blue circles) that their accretion histories intersect the critical mass curve: systems that cross the critical mass boundary earlier also start forming stars earlier. Indeed, the bottom (dashed) blue curve corresponds to a system that never crosses the critical boundary and that remains "dark" at $z = 0$. This result echoes earlier analyses reported by Fitts et al. (2017); Macciò et al. (2017); Benítez-Llambay and Fumagalli (2021).

Halos near the critical mass today, on average, follow the mass evolution of the critical mass. This implies that most halos that are today above critical have been so since early times, and similarly, most sub-critical halos today have always been below critical. The co-evolution of halo masses and the critical mass is also demonstrated by the grey histogram in the right-hand panel of Fig. 4.1, which shows the $z = 0$ halo mass distribution of all *luminous* galaxies in APOSTLE. The halo mass distribution has a clear peak at the present day critical mass $\sim 10^{9.7} M_\odot$, and a sharp decline towards lower masses. However, halos formed their stars in the past when the critical mass was lower, which requires that halos in this mass range followed on average the same mass-growth as the critical mass.

The decline in the number of halos hosting stellar populations below the critical mass may be attributed to the atypical accretion histories of halos in this mass range. In order for a halo to be luminous and sub-critical, it must have grown above critical at some point in their past history, before their mass growth slowed enough to fall under the critical boundary by the present time. One example of this is shown by the bottom solid blue curve in Fig. 4.1.

Similarly, in Fig. 4.4 there is also a small population of dwarfs that first ignited more recently, about 4-8 Gyrs ago.

4.1.3 Halo mass growth history and the modulation of star formation

The discussion of the previous section makes clear that the great majority of APOSTLE halos can only begin forming stars once their mass growth histories take them into the "above-critical" regime. However, it is not clear what happens if they happen to fall below critical at later times. We explore this in Figure 4.5, where we plot the mass accretion history of two illustrative examples. Blue solid curves indicate the mass evolution of the most massive progenitor, whereas the black dashed curve delineates the critical mass boundary. The orange curves track the gas content of each halo.

The blue shaded region brackets the interval between the youngest and oldest star formed in each system. The system on the left climbs above critical at $z \sim 7$ and remains so until the present. It starts forming stars soon after becoming critical and is still forming stars at $z = 0$. On the other hand, the example on the right depicts a halo that climbs above critical at $z \sim 6$ but becomes sub-critical soon thereafter, at $z \sim 2$. As the shaded region indicates, this halo only forms stars for as long as its mass remains above critical.

Note that the same process could, in principle, explain why some galaxies may stop forming stars for a relatively long time before reigniting, or why some have experienced several distinct episodes of star formation separated by quiescent periods. These cases have been reported in simulations by, e.g., Benítez-Llambay et al. (2015, 2016) and Rey et al. (2020), although Wright et al. (2019) interpreted their results in terms of environmental effects, rather than as a result of a critical mass imposed by the ionizing background.

The discussion above suggests that it is the interplay between mass growth history and the critical boundary that determines, to a large extent, the star formation activity of a dwarf. Feedback may also play a role, as seen by the sudden decrease in gas mass (orange line) that accompanies the onset of star formation (Fig. 4.5), but it appears to be less important overall: despite continuously forming stars, the system on the left-hand panel of Fig. 4.5 retains some gas (and forms stars) until today. This result suggests that the critical mass should delineate, on average, a clear boundary between star forming and quiescent systems.

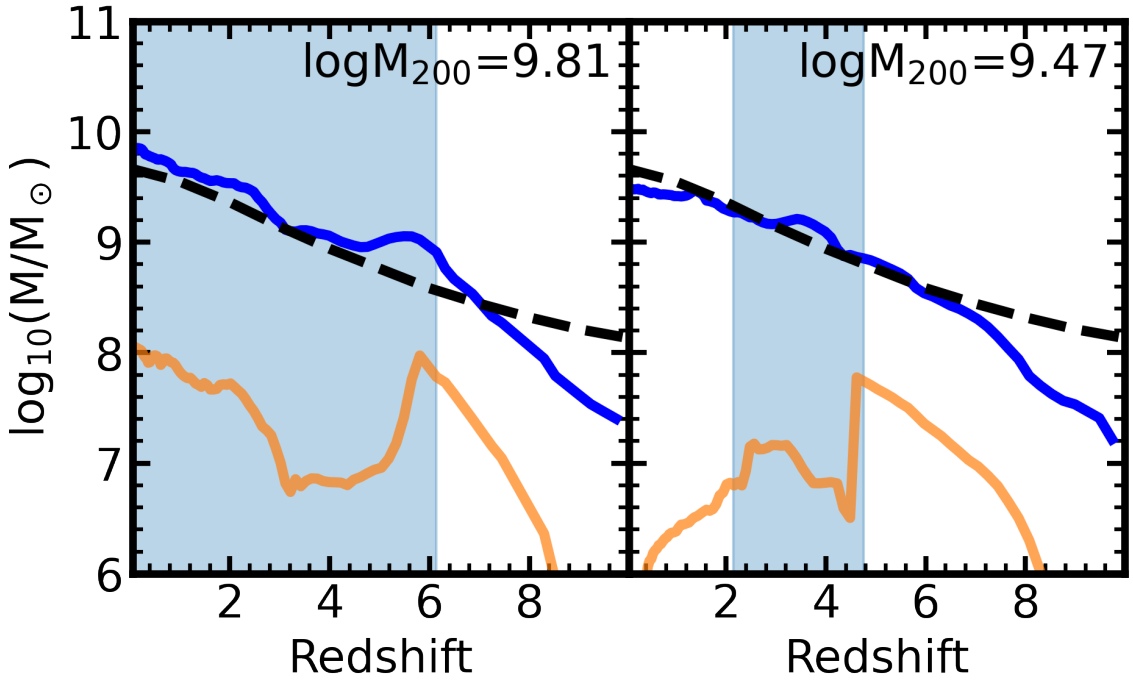

Figure 4.5: Mass assembly histories of two galaxies in the APOSTLE simulation, with masses at present day near the critical mass. The mass of the most massive progenitor is shown by the blue lines, and its gas mass in orange. The time interval over which a galaxy forms stars is shaded in blue, and is seen to coincide with the time the halo is above the critical boundary, shown by the dashed black curve.

4.2 Star forming vs quiescent dwarfs

We now examine the star forming properties of the field dwarf population in the APOSTLE simulation, which is shown in Fig. 4.6 at $z = 0$. The upper panel shows the stellar mass-halo mass relation, colored blue (star forming) if star formation is still ongoing and red (quiescent) if no stars have formed in the past 0.5 Gyrs. The vertical dashed line indicates the critical mass, and clearly separates the two dwarf populations: most halos above critical host galaxies where star formation is ongoing, whereas sub-critical halos host almost exclusively quiescent dwarfs. The distinction between these two populations is less clear using stellar mass, although there is a clear trend for the faintest dwarfs to be quiescent.

There have been a number of suggestions for truncating star formation in field dwarfs, notably the loss of its surrounding gaseous halo due to ram-pressure effects from the cosmic web (Benítez-Llambay et al. 2013) or from potential grazing passages through the virial radius of a more massive system (e.g., Teyssier et al. 2012). These may be contrasted with our scenario by examining the gas content of the quiescent population in APOSTLE, which would be largely absent if ram-pressure effects were the dominant mechanism. We explore this in Fig. 4.7, where we plot the gas mass of each APOSTLE central halo at $z = 0$ as a function of halo virial mass.

Blue and red circles indicate star forming and quiescent dwarfs, respectively, while the semi-transparent light-blue symbols indicate the (more numerous) "dark" REL-HIC systems. The green curve indicates, for reference, the total baryon mass of a halo, $f_{\rm bar} M_{200}$, whereas the cyan curve indicates the total gas mass expected by integrating eq. 3.3 for the gas density profile. As expected, the cyan curve tracks, on average, the total gas mass of a halo in the sub-critical regime.

Note that most quiescent galaxies still retain a large amount of gas, typically one or two orders of magnitude more than the stars they have been able to form. These systems thus appear to be quiescent not because of gas removal by feedback or environmental effects, but rather because their halo masses are below critical and thus unable to compress the gas to high enough central densities to ignite star formation.

This constitutes a robust and simple prediction of our model that should be testable by observations. In other words, our modeling predicts the existence of a sizable population of quiescent field dwarfs at the faint-end of the luminosity function. Such dwarfs are quite rare in the Local Group, with few known examples: the Cetus (Whiting et al. 1999) and Tucana (Lavery and Mighell 1992) dSphs, and

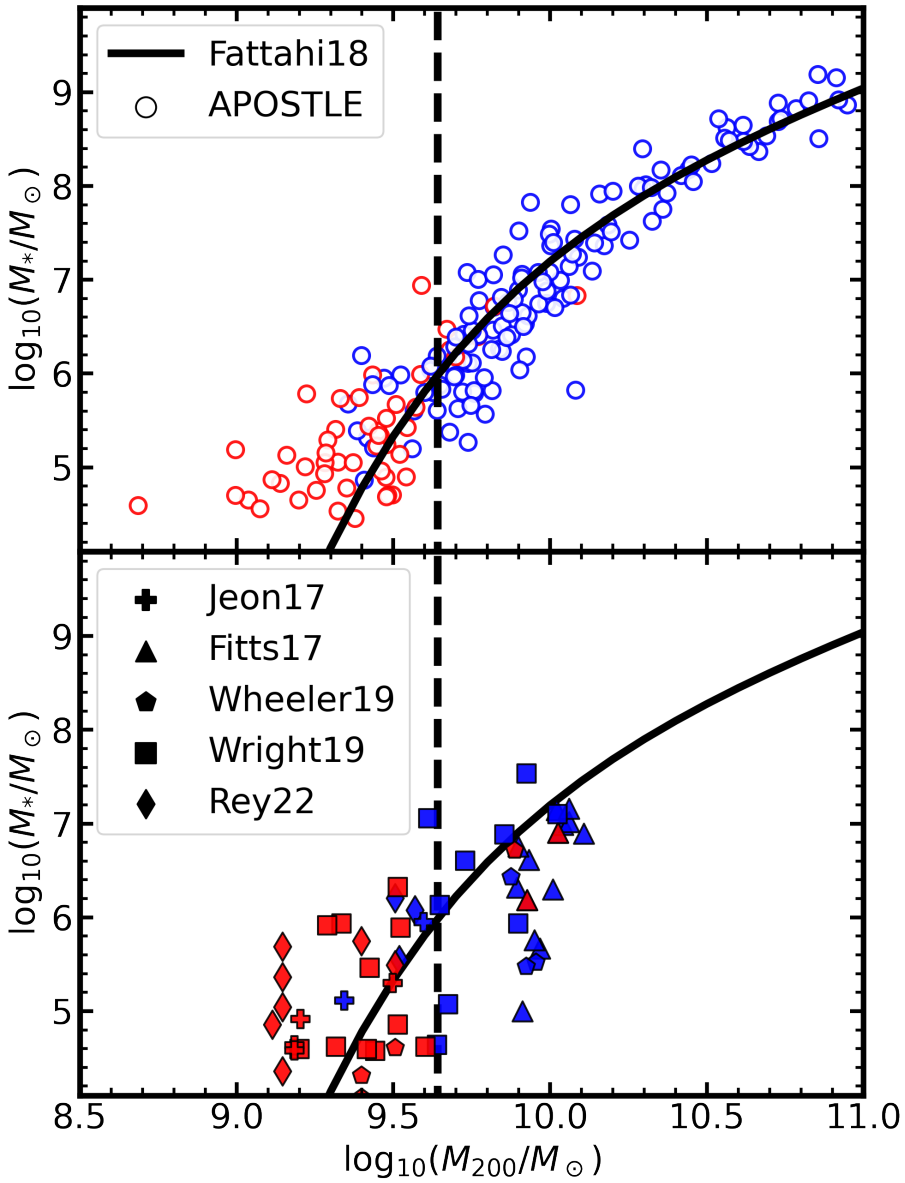

Figure 4.6: *Top:* Stellar mass of star forming (blue) and quiescent (red) galaxies in APOSTLE, as a function of virial mass at $z = 0$. For reference, the solid black curves show the APOSTLE M_*-M_{200} relation fit by Fattahi et al. (2018). *Bottom:* As top panel, but for recent cosmological hydrodynamical simulations of field dwarfs (Jeon et al. 2017; Fitts et al. 2017; Wheeler et al. 2019; Wright et al. 2019; Rey et al. 2022).

the more distant dwarfs, KKR 25 (Karachentsev et al. 2001; Makarov et al. 2012), KKs 3 (Karachentsev et al. 2015), and Andromeda XVIII (McConnachie et al. 2008; Makarova et al. 2017). They also seem to be rare in the local Universe; Geha et al. (2012) report the existence of a "threshold of $M_* < 10^9\,M_\odot$ below which quenched

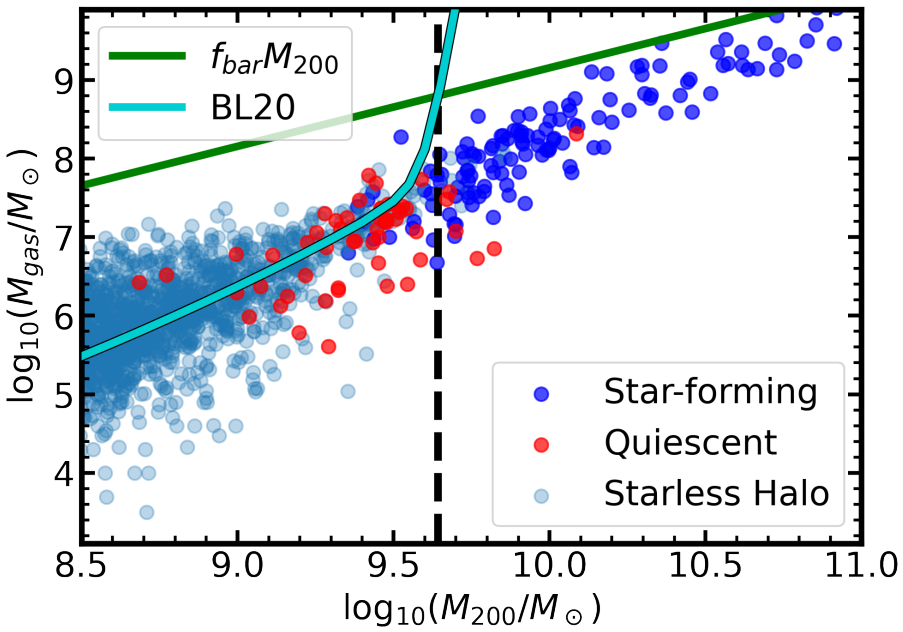

Figure 4.7: Gas mass within the virial radius of luminous dwarfs (star forming in blue; quiescent in red) and star-less halos (RELHICs, light blue) as a function of M_{200} at $z = 0$. Masses corresponding to the universal baryon fraction are shown by the green-line. The total gas mass expected for RELHICs from our modeling is shown by the cyan curve (see also Fig. 3.6).

galaxies do not exist in the field". Their survey, however, only extends down to $M_* > 10^7\,M_\odot$ before becoming severely incomplete. As shown in Fig. 4.6, the population of quiescent field dwarfs predicted by our analysis is expected to become prominent at much lower stellar masses.

APOSTLE is not the only simulation suite where these two populations of dwarfs have been seen. The bottom panel of Fig. 4.6 is analogous to the top, but includes results from five recent cosmological hydrodynamical simulations of dwarf galaxy formation (Jeon et al. 2017; Fitts et al. 2017; Wheeler et al. 2019; Wright et al. 2019; Rey et al. 2022), where the methodology for classifying these galaxies as star forming/quiescent classification is described in Appendix A. Remarkably, although each of these simulations adopt different recipes for star formation/feedback and disparate treatments of the interstellar medium, taken together they seem to agree with our main conclusion: there is a critical halo mass that separates star forming from quiescent dwarfs. Particularly, these simulations do not make use of the PEoS, and instead model the physics of a multi-phased ISM. Note again that the separation

is much less clear in M_* than it is in virial mass, highlighting the fact that it is the critical mass imposed by the ionizing UV background, and not stellar feedback, the main culprit for the origin of these two populations.

The existence of a population of faint, quiescent dwarfs inhabiting sub-critical halos is thus an intriguing prediction from our modeling that should be possible to verify in the near future. The quiescent isolated dwarf ($M_* \approx 2 \times 10^6\, M_\odot$) recently discovered by Polzin et al. (2021), together with the newly identified Tucana B ultra-faint dwarf (Sand et al. 2022), could very well be the archetypes of a whole population still awaiting discovery.

4.2.1 Star formation end times

As discussed in Sec. 1.1.2, cosmic reionization is often assumed to imply a sharp and very early truncation of star formation in faint dwarfs. Although this description may apply to low mass halos well below the critical boundary, we have seen that this is not the case for most field dwarfs inhabiting near-critical halos at $z = 0$. In such systems, the ionizing UV background seems to regulate the end of star formation somewhat indirectly, and in conjunction with the accretion history of a halo. It is therefore interesting to ask, for dwarfs that have ceased forming stars at present (i.e., those in "sub-critical" halos), when they experienced the last episode of star formation.

We show this in Fig. 4.8, where the red and blue histograms delineate the distribution of the youngest star particle in all APOSTLE galaxies with $M_{200} < 10^{11}\, M_\odot$ at $z = 0$. Those shaded in blue indicate star forming systems, whereas those in red correspond to the quiescent population at the present time. Clearly, there is a large diversity of "quenching" times, driven by the large diversity of individual halo mass accretion histories at fixed halo mass. This is another robust prediction for the quiescent population of isolated dwarfs that could be addressed in future observational studies.

4.2.2 Redshift dependence of the quiescent population

If our modeling is correct, then the quiescent population of dwarfs we discussed above should exist at all redshifts, although the boundary between quiescent and star forming should shift to lower masses at increasing redshift, tracking the evolution of the critical mass. We explore this in Fig. 4.9, where we show the differential halo mass function (averaged over the five APOSTLE volumes) at different redshifts. The

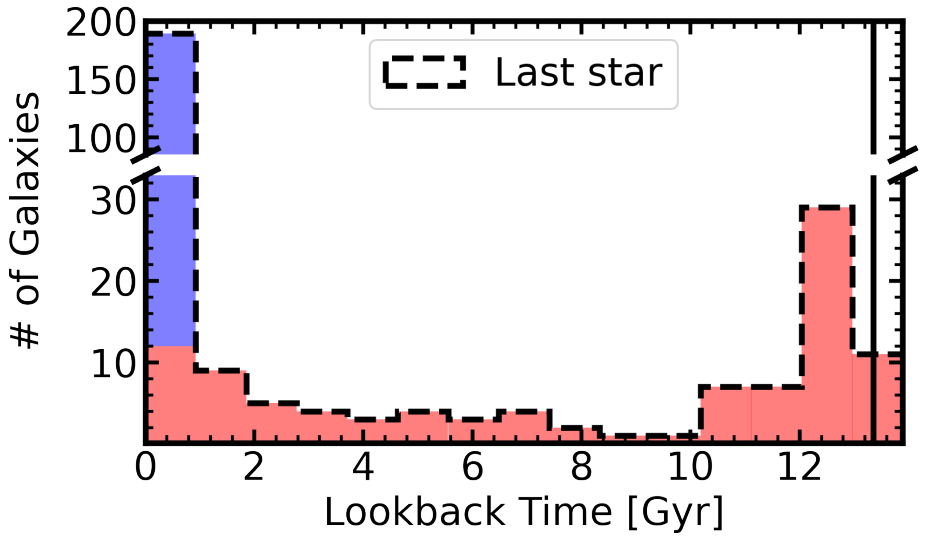

Figure 4.8: Age distribution of the youngest star particles in APOSTLE field dwarfs identified at $z = 0$ (grey data points in Fig. 4.1). Quiescent galaxies today (shaded in red) ceased forming stars over a wide range of times in the past.

solid black lines indicate the dark halo mass function, and the cyan curve denotes halos that have remained dark at each redshift. Green corresponds to all luminous galaxies, split between star forming (blue) and quiescent (i.e., those that did not form any stars in the most recent 0.5 Gyrs, in red) populations. The vertical dashed line indicates the critical mass according to our model (black curve in Fig. 3.8).

The quiescent population is mostly contained below the critical mass threshold at all redshifts, indicating that the critical mass model is still a valid threshold for star formation at other redshifts. The differentiation between populations becomes less neat at higher redshift, with an increasing function of sub-critical halos hosting star forming dwarfs. This is most likely because our definition of "star forming" uses a fixed time window of 0.5 Gyr to categorize systems, which represents a significant fraction of the universe's age at earlier times.

Another result illustrated by Fig. 4.9 is that, at all redshifts, $M_{\rm crit}$ represents a characteristic "threshold" for galaxy formation, in the sense that the fraction of "dark" halos grows sharply below that mass. Indeed, the number density of luminous galaxies peaks at about the critical mass, so that, in terms of sheer numbers, the majority of luminous field galaxies in any given volume should be faint dwarfs inhabiting halos near the critical boundary.

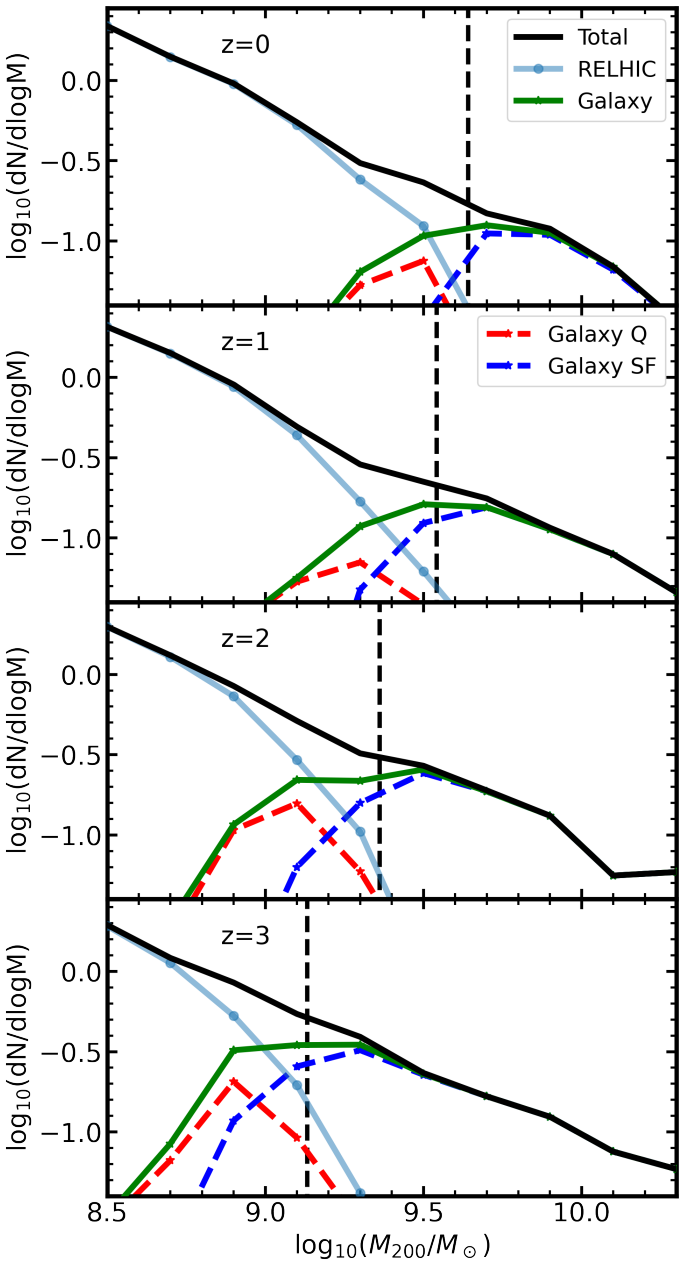

Figure 4.9: APOSTLE halo mass functions at different redshifts. Solid black lines indicate the halo mass function, averaged over the five APOSTLE volumes considered in this study. Star-less halos (RELHICs) are shown in light-blue, and galaxies in green. Galaxies are further subdivided into star forming (blue) and quiescent (red), with the critical mass at each redshift shown as a vertical dashed line.

4.3 Low-concentration Outliers

We return now to discuss the outlier population of low concentration halos which formed stars below the critical mass. We focus specifically on the low-concentration halos, because the existence of high-concentration halos forming stars below the critical mass line is not as unexpected, a result we demonstrated in section 4.1.1.

Fig. 4.10 shows a simplified version of Fig. 4.1, where only halos of concentration $c < 4$ which formed stars below the APOSTLE critical mass line are shown. These occurrences appear to be quite rare, with only 13 out of 2623 halos which started forming stars in isolation within all five APOSTLE volumes inspected. These objects were tracked individually, and they correspond to halos whose central gas densities are temporarily enhanced by passage through denser regions of the cosmic web, such as a filament or sheet of gas. This effect has already been noted by, eg. Benítez-Llambay et al. (2013); Wright et al. (2019).

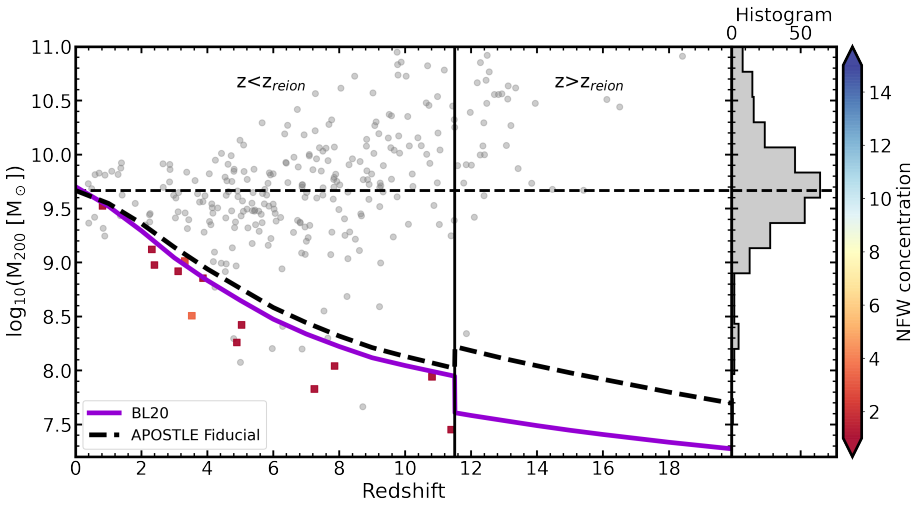

Figure 4.10: Simplified version of Fig. 4.1, where only halos with concentration $c < 4$ and which form stars below the APOSTLE critical mass (black-dashed) after reionization are shown.

The history of one such object is shown in Fig.4.11, where we show three snapshots, two preceding, and one immediately after the formation of the first star in the halo, all centered on the low-mass halo we are tracking. There is no significant evolution in the dark matter halo, shown in the left column, since its virial mass changes from $10^{8.41}$ to a maximum of $10^{8.59} M_\odot$, remaining below the critical mass at this redshift ($M_{\rm crit} \sim 10^{9.2} M_\odot$). However, shown in the right-hand column, this object

passes through a high density filament of gas, which is noticeable particularly in the $z = 3.98$ panel. The passage of the halo through the filament leaves in its wake a cometary tail of overdense gas. As the low-mass halo passes through the filament, its central gas is compressed and enables stars to form in this otherwise sub-critical halo. The evolution of the gas properties inside this halo are shown in Fig. 4.12, for the same three snapshots. The left column shows the temperature and density of all the gas particles in the volume shown as black-dots, and of the particles within the virial radius of the low mass halo as blue-dots. The same blue-dots are shown in isolation in the right-hand column. The main evolution over the three snapshots is the increase in the maximum density reached by gas particles within the virial radius of the low-mass halo. However, the snapshot in which a gas particle crossed the density threshold for star formation was not recorded. This suggests that the increase in density above critical occurred between two output snapshots of the APOSTLE simulation, which were written 53 Myrs apart.

The other low-concentration outliers follow similar circumstances at the moment they begin forming stars, while passing through a region of space with higher than average gas density. This set of circumstances does not appear to be very common in the Local Group field, as only 13 such objects were found in the five APOSTLE volumes, but may be a more significant dynamic for halos that are being accreted onto a more massive objects, such as the Milky Way and Andromeda. Satellite galaxies were intentionally excluded from our analysis since we have restricted our analysis to isolated dwarfs. However, it is conceivable that on the first pericentric passage of a subhalo, prior to gas being completely removed via ram-pressure stripping, the same force may compress the gas in the central region and allow for star formation to briefly occur in a sub-critical halo (eg. Di Cintio et al. 2021). This mechanism might have a significant effect on the distribution of star forming/quiescent predicted by this work, particularly for the population of dwarf-galaxies at the boundary of the Milky Way and the field.

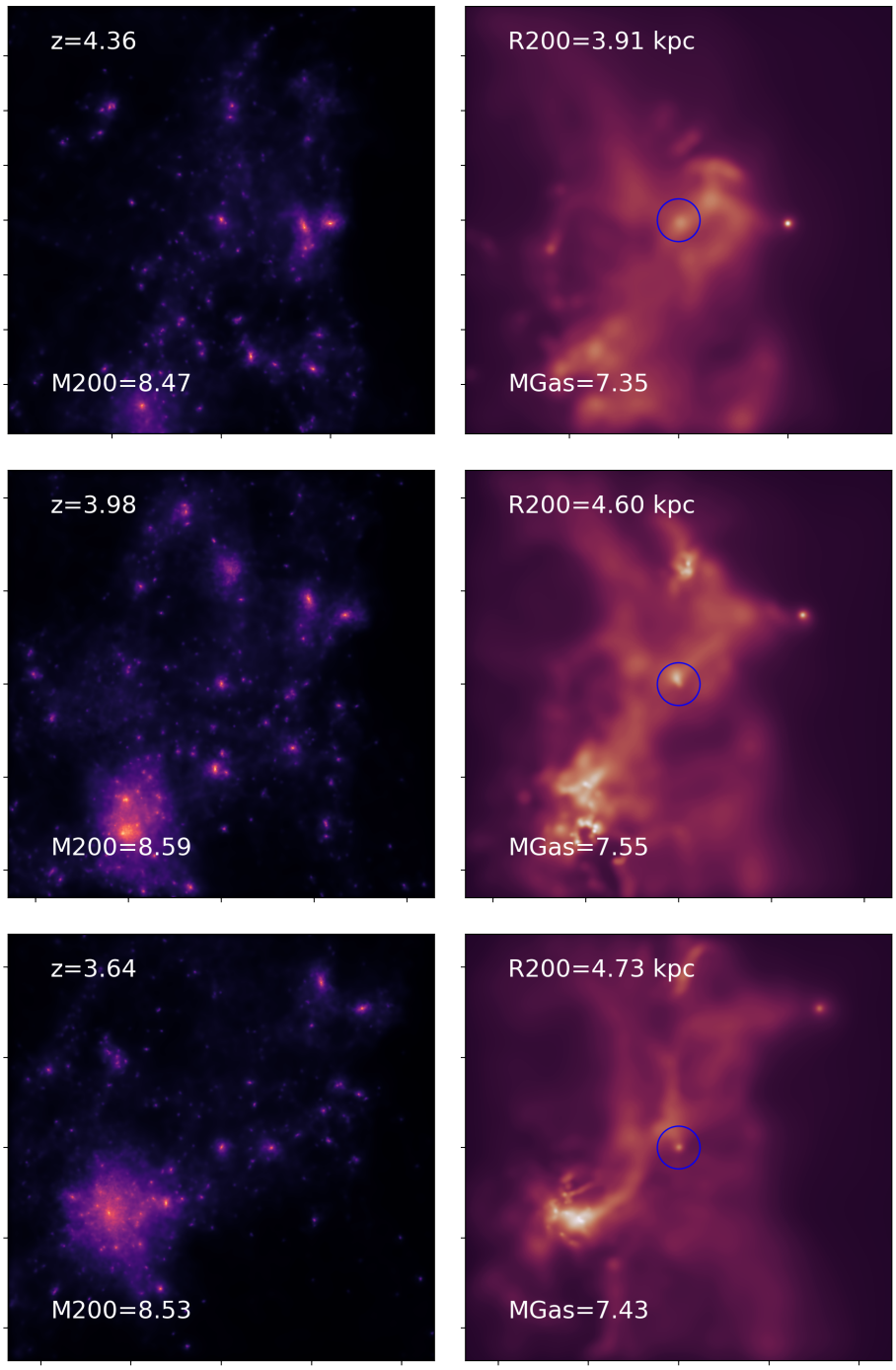

Figure 4.11: Evolution of a single low concentration halo from $z = 4.36$ until it formed its first star, at $z = 3.64$. The *left* column shows the dark matter particle distribution, and the *right* column the gas particles, both centered on the same halo. The blue circle in the gas particle plot shows the virial radius of the halo, with its physical extended labelled as $R200$ on the same plot.

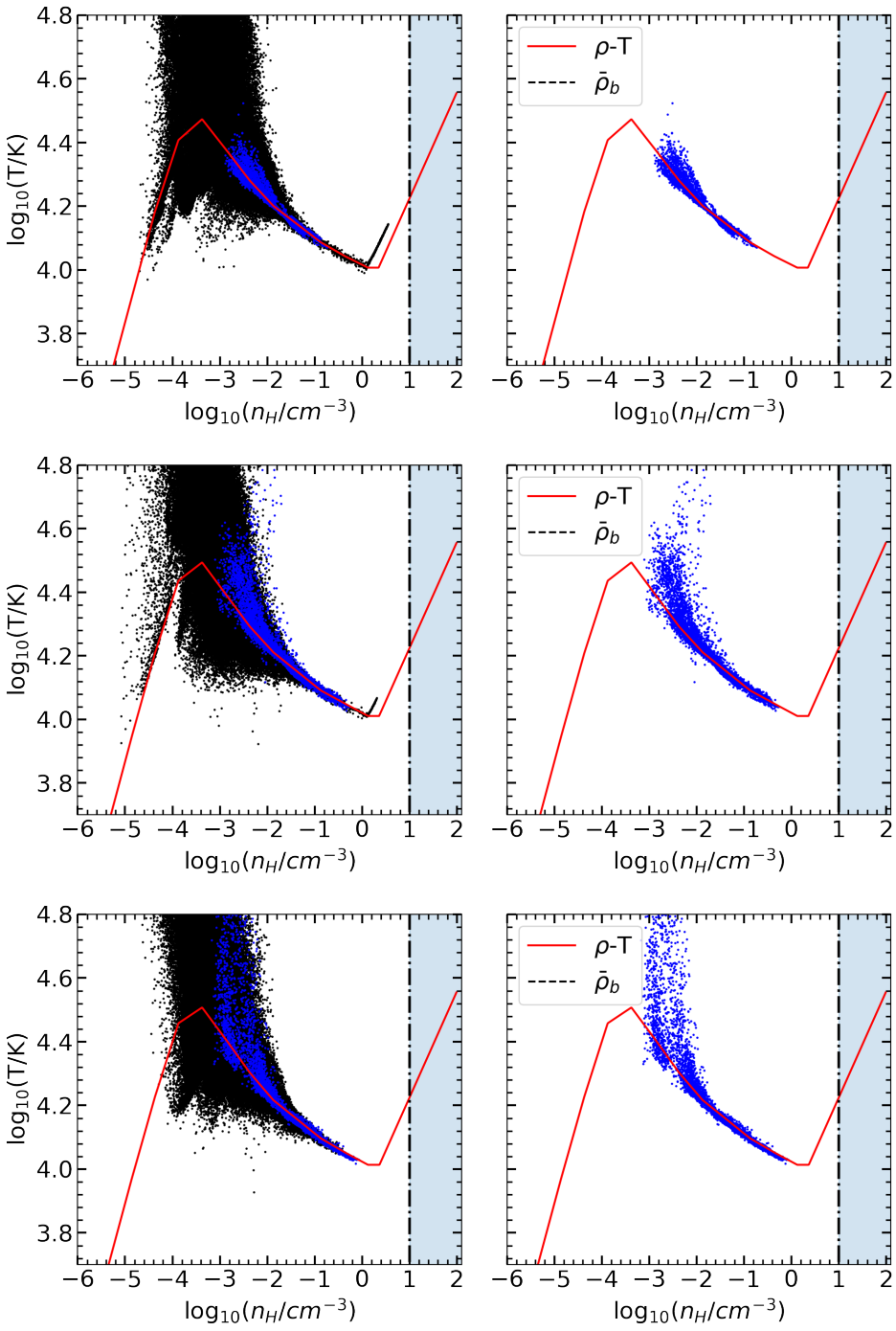

Figure 4.12: Temperature and density of gas particles from the snapshots shown in Fig. 4.11 where black-dots represent any particle within the volume shown, and blue-dots indicate that the particles are within the virial radius of the low-mass halo that formed stars. The solid-red line shows the temperature-density relation at that redshift, and densities above the star formation threshold of APOSTLE are highlighted by the blue-shaded region.

Chapter 5

Summary

We have examined the onset of star formation in low-mass halos identified in the APOSTLE cosmological hydrodynamical simulations. Star formation begins once the mass of a halo reaches a characteristic "critical" mass that may be derived using a simple model that combines the NFW mass profile of LCDM halos and the thermodynamics of gas heated by the cosmic ionizing background.

The model assumes hydrostatic equilibrium to derive the gas density profile at various redshifts, and identifies the critical mass where the central gas density equals the gas density threshold for star formation adopted in the APOSTLE simulation. This redshift-dependent critical mass, grows from $\sim 10^8$ at $z = 11.5$ to $\sim 10^{9.7} M_\odot$ by present day, and describes quite accurately the minimum virial mass needed for a halo to first ignite its star formation activity, especially after reionization.

The model predicts that star formation never takes place in halos that remain subcritical, and ceases if the halo mass drops below critical, in excellent agreement with APOSTLE simulation results, as well as those of other recent cosmological hydrodynamical simulations. The ionizing background thus seems to be the main mechanism regulating star formation in field dwarf galaxies, through the interplay between the critical mass boundary and the mass accretion history of a dwarf's dark matter halo.

A few notable results of our analysis may be summarized as follows.

- The scatter in virial mass at the onset of star formation is tightly correlated with halo concentration, as expected from our critical mass model. However, the lowest concentration halos tend to exceed the virial mass predicted by the critical mass model. This may be due to a "delay-time" between a halo crossing the critical mass and the onset of star formation, which coupled with a concen-

tration dependent mass assembly history, can result in the lowest concentration halos growing well above the critical mass before forming their first star.

- The evolution of the critical mass with time is roughly parallel to the average mass accretion history of halos near the critical regime, implying that, in general, halos above- or sub-critical at present have remained so since early times. This implies in a sharp decrease in the fraction of halos harboring luminous systems below the critical mass at $z = 0$.

- For the same reason, dwarf galaxies at $z = 0$, regardless of their luminosity, became able to form stars quite early, providing a simple and appealing explanation for the ubiquitous presence of ancient stellar populations in all known dwarfs.

- Sub-critical halos can still host luminous galaxies, but only if they were above critical at some point in the past. However, they are expected to be quiescent, forming a sizable population of non-star forming dwarfs at the very faint end of the field galaxy stellar mass function. Very few such galaxies have been discovered in the field so far, but the discovery of this population would provide strong evidence in support of this scenario.

- Halos whose accretion histories cross the critical boundary several times during their evolution may host several distinct episodes of star formation, without need for environmental effects, a result that may help to explain the puzzlingly episodic nature of star formation observed in some dwarfs.

Although this simple scenario accounts for the main features of the star formation history of the faintest dwarfs in APOSTLE, it is important to note some of its caveats and limitations as well. We have focused exclusively on isolated systems, mainly because of simplicity, but note that environmental effects such as ram-pressure and tidal stripping may dominate in dwarfs that are satellites of more massive systems.

Particularly, it was noted that systems interacting with high density filaments of gas were capable of triggering star formation even if the halo was sub-critical. This may have strong implications for the population of sub-critical halos interacting for the first time with the high-density circum galactic medium of the Milky Way, and their star formation properties. Therefore, it is important to exercise care when applying these results to the interpretation of the star formation histories of dwarfs in

the Local Group, where satellites make up the majority of systems studied observationally in detail so far.

We also note that the use of a "polytropic equation of state" (PEoS) in APOSTLE artificially reduces the ability of low-mass halos to form stars prior to reionization. This rather crude numerical treatment of high-density gas means that our conclusions, however appealing, must be treated with care, and should be scrutinized further in future simulation work with more sophisticated treatments of the interstellar medium. Nevertheless, we believe that many of the conclusions highlighted above will prove of lasting value, and will provide a useful interpretive framework for future work.

5.1 Future Work

The analysis presented in this thesis provides an interesting framework with which to study the population of star forming and quiescent field dwarf galaxies in the Local Group.

A natural continuation of this work would be to study how the evolving critical mass couples to the diversity of star formation histories observed for dwarf galaxies of the Local Group. In particular, this model may be used to explain the episodic star formation and some dwarf galaxies, in the context of excursions in the halo mass above the critical regime.

However, there are some valid questions about whether the assumptions made for starless dark matter halos, needed to calculate the critical mass, should also apply to halos with stars - ie. galaxies. Two questions in particular stand out, 1) how significant is the feedback from the stellar population in these low mass dark matter halos, and therefore the deviation from hydrostatic equilibrium assumed, and 2) how significant is the metal enrichment of gas in these halos, and does it alter the $T-\rho$ relation which we used, from Fig. 3.2. These two mechanisms are included in the APOSTLE simulation, and the simulation's results appear to match very well with the critical mass model. However, the deviation from hydrostatic equilibrium caused by stellar feedback would work to increase the critical mass, while the metalicity enhancement, by increasing radiative cooling, would decrease the critical mass. It remains a possibility that these two mechanisms can, individually, have a non-negligible effect on the critical mass, but when added together, they produce a critical mass in APOSTLE that is similar to the one obtained under the assumption of hydrostatic equilibrium and primordial gas composition.

Additionally, the observed excess in virial mass of low-concentration halos in APOSTLE compared to the critical mass raised the hypothesis of a "delay time" between the moment a halo grows above critical and the onset of star formation. The timescale of a "delay time" may be estimated using dynamical or sound-crossing arguments, and be used to test if this hypothesis is valid. This would be easily implemented within the mass assembly history analysis we provided (discussed in section 4.1.1).

With our analysis, it also appears that the critical mass value at present day is applicable to a diverse set of cosmological simulations, which treated the multi-phase ISM in more detail than APOSTLE. However, this agreement was only visible for the aggregate of different cosmological simulations, each with differing treatments of the ISM, with the possibility still existing that each simulation will have a slightly different critical mass than the APOSTLE simulation. It is therefore a natural extension of this work, to study the onset of star formation with other simulation codes, which extend the $T-\rho$ relation to higher densities and including the physics of self-shielding.

Additionally, a better understanding is also needed of the critical mass threshold prior to reionization. In APOSTLE, the Polytropic Equation of State imposed on the $T-\rho$ relation appeared to suppress star formation by nearly 1 order of magnitude in halo masses when compared to the atomic cooling limit.

Once the baryonic processes are more thoroughly understood, this model is ultimately also a test of LCDM cosmology and the structure of dark matter on the smallest scales. In practice, the shape of the dark matter profile may be tested, because of changes expected for the critical mass if the profile is cored, as is the case for self-interacting dark matter models, or if the average halo concentration is lower, which is expected for warm dark matter.

Bibliography

Abadi, M. G., Moore, B., and Bower, R. G. (1999). Ram pressure stripping of spiral galaxies in clusters. , 308(4):947–954.

Balogh, M. L., Navarro, J. F., and Morris, S. L. (2000). The Origin of Star Formation Gradients in Rich Galaxy Clusters. , 540(1):113–121.

Barkana, R. and Loeb, A. (2001). In the beginning: the first sources of light and the reionization of the universe. , 349(2):125–238.

Behroozi, P. S., Conroy, C., and Wechsler, R. H. (2010). A Comprehensive Analysis of Uncertainties Affecting the Stellar Mass-Halo Mass Relation for 0 ¡ z ¡ 4. , 717(1):379–403.

Benítez-Llambay, A. (2017). Py-SPHViewer: Cosmological simulations using Smoothed Particle Hydrodynamics. Astrophysics Source Code Library, record ascl:1712.003.

Benítez-Llambay, A. and Frenk, C. (2020). The detailed structure and the onset of galaxy formation in low-mass gaseous dark matter haloes. , 498(4):4887–4900.

Benítez-Llambay, A. and Fumagalli, M. (2021). The Tail of Late-forming Dwarf Galaxies in ΛCDM. , 921(1):L9.

Benítez-Llambay, A., Navarro, J. F., Abadi, M. G., Gottlöber, S., Yepes, G., Hoffman, Y., and Steinmetz, M. (2013). Dwarf Galaxies and the Cosmic Web. , 763(2):L41.

Benítez-Llambay, A., Navarro, J. F., Abadi, M. G., Gottlöber, S., Yepes, G., Hoffman, Y., and Steinmetz, M. (2015). The imprint of reionization on the star formation histories of dwarf galaxies. , 450(4):4207–4220.

Benítez-Llambay, A., Navarro, J. F., Abadi, M. G., Gottlöber, S., Yepes, G., Hoffman, Y., and Steinmetz, M. (2016). Mergers and the outside-in formation of dwarf spheroidals. , 456(2):1185–1194.

Benítez-Llambay, A., Navarro, J. F., Frenk, C. S., Sawala, T., Oman, K., Fattahi, A., Schaller, M., Schaye, J., Crain, R. A., and Theuns, T. (2017). The properties of 'dark' ΛCDM haloes in the Local Group. , 465(4):3913–3926.

Benson, A. J., Lacey, C. G., Baugh, C. M., Cole, S., and Frenk, C. S. (2002). The effects of photoionization on galaxy formation - I. Model and results at z=0. , 333(1):156–176.

Bromm, V. and Yoshida, N. (2011). The First Galaxies. , 49(1):373–407.

Brown, T. M., Tumlinson, J., Geha, M., Simon, J. D., Vargas, L. C., VandenBerg, D. A., Kirby, E. N., Kalirai, J. S., Avila, R. J., Gennaro, M., Ferguson, H. C., Muñoz, R. R., Guhathakurta, P., and Renzini, A. (2014). The Quenching of the Ultra-faint Dwarf Galaxies in the Reionization Era. , 796(2):91.

Bullock, J. S. and Boylan-Kolchin, M. (2017). Small-Scale Challenges to the ΛCDM Paradigm. , 55(1):343–387.

Bullock, J. S., Kravtsov, A. V., and Weinberg, D. H. (2000). Reionization and the abundance of galactic satellites. , 539(2):517–521.

Bullock, J. S., Kravtsov, A. V., and Weinberg, D. H. (2001). Hierarchical Galaxy Formation and Substructure in the Galaxy's Stellar Halo. , 548(1):33–46.

Carignan, C. and Freeman, K. C. (1988). DDO 154: A "Dark" Galaxy? , 332:L33.

Chabrier, G. (2003). Galactic Stellar and Substellar Initial Mass Function. , 115(809):763–795.

Chiba, M. and Nath, B. B. (1994). Effects of Photoionization on Galaxy Formation. , 436:618.

Clowe, D., Bradač, M., Gonzalez, A. H., Markevitch, M., Randall, S. W., Jones, C., and Zaritsky, D. (2006). A Direct Empirical Proof of the Existence of Dark Matter. , 648(2):L109–L113.

Couchman, H. M. P. and Rees, M. J. (1986). Pregalactic evolution in cosmologies with cold dark matter. , 221:53–62.

Crain, R. A., Schaye, J., Bower, R. G., Furlong, M., Schaller, M., Theuns, T., Dalla Vecchia, C., Frenk, C. S., McCarthy, I. G., Helly, J. C., Jenkins, A., Rosas-Guevara, Y. M., White, S. D. M., and Trayford, J. W. (2015). The EAGLE simulations of galaxy formation: calibration of subgrid physics and model variations. , 450(2):1937–1961.

Dalla Vecchia, C. and Schaye, J. (2012). Simulating galactic outflows with thermal supernova feedback. , 426(1):140–158.

Davis, M., Efstathiou, G., Frenk, C. S., and White, S. D. M. (1985). The evolution of large-scale structure in a universe dominated by cold dark matter. , 292:371–394.

Dawoodbhoy, T., Shapiro, P. R., Ocvirk, P., Aubert, D., Gillet, N., Choi, J.-H., Iliev, I. T., Teyssier, R., Yepes, G., Gottlöber, S., D'Aloisio, A., Park, H., and Hoffman, Y. (2018). Suppression of star formation in low-mass galaxies caused by the reionization of their local neighbourhood. , 480(2):1740–1753.

Di Cintio, A., Brook, C. B., Macciò, A. V., Stinson, G. S., Knebe, A., Dutton, A. A., and Wadsley, J. (2014). The dependence of dark matter profiles on the stellar-to-halo mass ratio: a prediction for cusps versus cores. , 437(1):415–423.

Di Cintio, A., Mostoghiu, R., Knebe, A., and Navarro, J. F. (2021). Pericentric passage-driven star formation in satellite galaxies and their hosts: CLUES from local group simulations. , 506(1):531–545.

Digby, R., Navarro, J. F., Fattahi, A., Simpson, C. M., Oman, K. A., Gomez, F. A., Frenk, C. S., Grand, R. J. J., and Pakmor, R. (2019). The star formation histories of dwarf galaxies in Local Group cosmological simulations. , 485(4):5423–5437.

Dolag, K., Borgani, S., Murante, G., and Springel, V. (2009). Substructures in hydrodynamical cluster simulations. , 399(2):497–514.

Efstathiou, G. (1992). Suppressing the formation of dwarf galaxies via photoionization. , 256(1):43P–47P.

Evrard, A. E., Metzler, C. A., and Navarro, J. F. (1996). Mass Estimates of X-Ray Clusters. , 469:494.

Fattahi, A., Navarro, J. F., and Frenk, C. S. (2020). The missing dwarf galaxies of the Local Group. , 493(2):2596–2605.

Fattahi, A., Navarro, J. F., Frenk, C. S., Oman, K. A., Sawala, T., and Schaller, M. (2018). Tidal stripping and the structure of dwarf galaxies in the Local Group. , 476(3):3816–3836.

Fattahi, A., Navarro, J. F., Sawala, T., Frenk, C. S., Oman, K. A., Crain, R. A., Furlong, M., Schaller, M., Schaye, J., Theuns, T., and Jenkins, A. (2016). The APOSTLE project: Local Group kinematic mass constraints and simulation candidate selection. , 457(1):844–856.

Ferland, G. J., Korista, K. T., Verner, D. A., Ferguson, J. W., Kingdon, J. B., and Verner, E. M. (1998). CLOUDY 90: Numerical Simulation of Plasmas and Their Spectra. , 110(749):761–778.

Fitts, A., Boylan-Kolchin, M., Elbert, O. D., Bullock, J. S., Hopkins, P. F., Oñorbe, J., Wetzel, A., Wheeler, C., Faucher-Giguère, C.-A., Kereš, D., Skillman, E. D., and Weisz, D. R. (2017). fire in the field: simulating the threshold of galaxy formation. , 471(3):3547–3562.

Frenk, C. S. and White, S. D. M. (2012). Dark matter and cosmic structure. *Annalen der Physik*, 524(9-10):507–534.

Gallart, C., Monelli, M., Mayer, L., Aparicio, A., Battaglia, G., Bernard, E. J., Cassisi, S., Cole, A. A., Dolphin, A. E., Drozdovsky, I., Hidalgo, S. L., Navarro, J. F., Salvadori, S., Skillman, E. D., Stetson, P. B., and Weisz, D. R. (2015). The ACS LCID Project: On the Origin of Dwarf Galaxy Types—A Manifestation of the Halo Assembly Bias? , 811(2):L18.

Geha, M., Blanton, M. R., Yan, R., and Tinker, J. L. (2012). A Stellar Mass Threshold for Quenching of Field Galaxies. , 757(1):85.

Gill, S. P. D., Knebe, A., and Gibson, B. K. (2005). The evolution of substructure - III. The outskirts of clusters. , 356(4):1327–1332.

Gnedin, N. Y. (2000). Effect of Reionization on Structure Formation in the Universe. , 542(2):535–541.

Gnedin, O. Y., Kravtsov, A. V., Klypin, A. A., and Nagai, D. (2004). Response of Dark Matter Halos to Condensation of Baryons: Cosmological Simulations and Improved Adiabatic Contraction Model. , 616(1):16–26.

Gnedin, O. Y. and Zhao, H. (2002). Maximum feedback and dark matter profiles of dwarf galaxies. , 333(2):299–306.

Governato, F., Brook, C., Mayer, L., Brooks, A., Rhee, G., Wadsley, J., Jonsson, P., Willman, B., Stinson, G., Quinn, T., and Madau, P. (2010). Bulgeless dwarf galaxies and dark matter cores from supernova-driven outflows. , 463(7278):203–206.

Gunn, J. E. and Gott, J. Richard, I. (1972). On the Infall of Matter Into Clusters of Galaxies and Some Effects on Their Evolution. , 176:1.

Haardt, F. and Madau, P. (2001). Modelling the UV/X-ray cosmic background with CUBA. In Neumann, D. M. and Tran, J. T. V., editors, *Clusters of Galaxies and the High Redshift Universe Observed in X-rays*, page 64.

Haehnelt, M. G., Steinmetz, M., and Rauch, M. (1996). C IV Absorption from Galaxies in the Process of Formation. , 465:L95.

Hodge, P. W. (1971). Dwarf Galaxies. , 9:35.

Hopkins, P. F. (2013). A general class of Lagrangian smoothed particle hydrodynamics methods and implications for fluid mixing problems. , 428(4):2840–2856.

Ikeuchi, S. (1986). The baryon clump within an extended dark matter region. , 118(1-2):509–514.

Jenkins, A. (2013). A new way of setting the phases for cosmological multiscale Gaussian initial conditions. , 434(3):2094–2120.

Jeon, M., Besla, G., and Bromm, V. (2017). Connecting the First Galaxies with Ultrafaint Dwarfs in the Local Group: Chemical Signatures of Population III Stars. , 848(2):85.

Karachentsev, I. D., Makarova, L. N., Makarov, D. I., Tully, R. B., and Rizzi, L. (2015). A new isolated dSph galaxy near the Local Group. , 447(1):L85–L89.

Karachentsev, I. D., Sharina, M. E., Dolphin, A. E., Geisler, D., Grebel, E. K., Guhathakurta, P., Hodge, P. W., Karachentseva, V. E., Sarajedini, A., and Seitzer, P. (2001). A new galaxy near the Local Group in Draco. , 379:407–411.

Katz, N. and White, S. D. M. (1993). Hierarchical Galaxy Formation: Overmerging and the Formation of an X-Ray Cluster. , 412:455.

Klypin, A., Kravtsov, A. V., Valenzuela, O., and Prada, F. (1999). Where are the missing galactic satellites? , 522(1):82–92.

Komatsu, E., Smith, K. M., Dunkley, J., Bennett, C. L., Gold, B., Hinshaw, G., Jarosik, N., Larson, D., Nolta, M. R., Page, L., Spergel, D. N., Halpern, M., Hill, R. S., Kogut, A., Limon, M., Meyer, S. S., Odegard, N., Tucker, G. S., Weiland, J. L., Wollack, E., and Wright, E. L. (2011). Seven-year Wilkinson Microwave Anisotropy Probe (WMAP) Observations: Cosmological Interpretation. , 192(2):18.

Kravtsov, A. V., Gnedin, O. Y., and Klypin, A. A. (2004). The Tumultuous Lives of Galactic Dwarfs and the Missing Satellites Problem. , 609(2):482–497.

Kulkarni, M., Visbal, E., and Bryan, G. L. (2021). The Critical Dark Matter Halo Mass for Population III Star Formation: Dependence on Lyman-Werner Radiation, Baryon-dark Matter Streaming Velocity, and Redshift. , 917(1):40.

Lavery, R. J. and Mighell, K. J. (1992). A New Member of the Local Group: The Tucana Dwarf Galaxy. , 103:81.

Ludlow, A. D., Bose, S., Angulo, R. E., Wang, L., Hellwing, W. A., Navarro, J. F., Cole, S., and Frenk, C. S. (2016). The mass-concentration-redshift relation of cold and warm dark matter haloes. , 460(2):1214–1232.

Macciò, A. V., Frings, J., Buck, T., Penzo, C., Dutton, A. A., Blank, M., and Obreja, A. (2017). The edge of galaxy formation - I. Formation and evolution of MW-satellite analogues before accretion. , 472(2):2356–2366.

Madau, P. and Dickinson, M. (2014). Cosmic Star-Formation History. , 52:415–486.

Makarov, D., Makarova, L., Sharina, M., Uklein, R., Tikhonov, A., Guhathakurta, P., Kirby, E., and Terekhova, N. (2012). A unique isolated dwarf spheroidal galaxy at D = 1.9 Mpc. , 425(1):709–719.

Makarova, L. N., Makarov, D. I., Karachentsev, I. D., Tully, R. B., and Rizzi, L. (2017). Star formation history of And XVIII: a dwarf spheroidal galaxy in isolation. , 464(2):2281–2289.

Mayer, L., Governato, F., Colpi, M., Moore, B., Quinn, T., Wadsley, J., Stadel, J., and Lake, G. (2001). Tidal Stirring and the Origin of Dwarf Spheroidals in the Local Group. , 547(2):L123–L127.

McConnachie, A. W. (2012). The Observed Properties of Dwarf Galaxies in and around the Local Group. , 144(1):4.

McConnachie, A. W., Huxor, A., Martin, N. F., Irwin, M. J., Chapman, S. C., Fahlman, G., Ferguson, A. M. N., Ibata, R. A., Lewis, G. F., Richer, H., and Tanvir, N. R. (2008). A Trio of New Local Group Galaxies with Extreme Properties. , 688(2):1009–1020.

Moore, B., Ghigna, S., Governato, F., Lake, G., Quinn, T., Stadel, J., and Tozzi, P. (1999a). Dark Matter Substructure within Galactic Halos. , 524(1):L19–L22.

Moore, B., Quinn, T., Governato, F., Stadel, J., and Lake, G. (1999b). Cold collapse and the core catastrophe. , 310(4):1147–1152.

Mortlock, D. J., Warren, S. J., Venemans, B. P., Patel, M., Hewett, P. C., McMahon, R. G., Simpson, C., Theuns, T., Gonzáles-Solares, E. A., Adamson, A., Dye, S., Hambly, N. C., Hirst, P., Irwin, M. J., Kuiper, E., Lawrence, A., and Röttgering, H. J. A. (2011). A luminous quasar at a redshift of z = 7.085. , 474(7353):616–619.

Moster, B. P., Somerville, R. S., Maulbetsch, C., van den Bosch, F. C., Macciò, A. V., Naab, T., and Oser, L. (2010). Constraints on the Relationship between Stellar Mass and Halo Mass at Low and High Redshift. , 710(2):903–923.

Murray, S. G., Power, C., and Robotham, A. S. G. (2013). How well do we know the halo mass function ? , 434:L61–L65.

Navarro, J. F., Eke, V. R., and Frenk, C. S. (1996a). The cores of dwarf galaxy haloes. , 283(3):L72–L78.

Navarro, J. F., Frenk, C. S., and White, S. D. M. (1996b). The Structure of Cold Dark Matter Halos. , 462:563.

Navarro, J. F., Frenk, C. S., and White, S. D. M. (1997). A Universal Density Profile from Hierarchical Clustering. , 490(2):493–508.

Navarro, J. F. and Steinmetz, M. (1997). The Effects of a Photoionizing Ultraviolet Background on the Formation of Disk Galaxies. , 478(1):13–28.

Oh, S. P. and Haiman, Z. (2002). Second-generation objects in the universe: Radiative cooling and collapse of halos with virial temperatures above 10sup4/supk. , 569(2):558–572.

Okamoto, T., Gao, L., and Theuns, T. (2008). Mass loss of galaxies due to an ultraviolet background. , 390(3):920–928.

Oman, K. A., Navarro, J. F., Fattahi, A., Frenk, C. S., Sawala, T., White, S. D. M., Bower, R., Crain, R. A., Furlong, M., Schaller, M., Schaye, J., and Theuns, T. (2015). The unexpected diversity of dwarf galaxy rotation curves. , 452(4):3650–3665.

Omukai, K. and Palla, F. (2003). Formation of the First Stars by Accretion. , 589(2):677–687.

Percival, W. J., Reid, B. A., Eisenstein, D. J., Bahcall, N. A., Budavari, T., Frieman, J. A., Fukugita, M., Gunn, J. E., Ivezić, Ž., Knapp, G. R., Kron, R. G., Loveday, J., Lupton, R. H., McKay, T. A., Meiksin, A., Nichol, R. C., Pope, A. C., Schlegel, D. J., Schneider, D. P., Spergel, D. N., Stoughton, C., Strauss, M. A., Szalay, A. S., Tegmark, M., Vogeley, M. S., Weinberg, D. H., York, D. G., and Zehavi, I. (2010). Baryon acoustic oscillations in the Sloan Digital Sky Survey Data Release 7 galaxy sample. , 401(4):2148–2168.

Planck Collaboration, Aghanim, N., Akrami, Y., Ashdown, M., Aumont, J., Baccigalupi, C., Ballardini, M., Banday, A. J., Barreiro, R. B., Bartolo, N., Basak, S., Battye, R., Benabed, K., Bernard, J. P., Bersanelli, M., Bielewicz, P., Bock, J. J., Bond, J. R., Borrill, J., Bouchet, F. R., Boulanger, F., Bucher, M., Burigana, C., Butler, R. C., Calabrese, E., Cardoso, J. F., Carron, J., Challinor, A., Chiang, H. C., Chluba, J., Colombo, L. P. L., Combet, C., Contreras, D., Crill, B. P., Cuttaia, F., de Bernardis, P., de Zotti, G., Delabrouille, J., Delouis, J. M., Di Valentino, E., Diego, J. M., Doré, O., Douspis, M., Ducout, A., Dupac, X., Dusini, S., Efstathiou, G., Elsner, F., Enßlin, T. A., Eriksen, H. K., Fantaye, Y.,

Farhang, M., Fergusson, J., Fernandez-Cobos, R., Finelli, F., Forastieri, F., Frailis, M., Fraisse, A. A., Franceschi, E., Frolov, A., Galeotta, S., Galli, S., Ganga, K., Génova-Santos, R. T., Gerbino, M., Ghosh, T., González-Nuevo, J., Górski, K. M., Gratton, S., Gruppuso, A., Gudmundsson, J. E., Hamann, J., Handley, W., Hansen, F. K., Herranz, D., Hildebrandt, S. R., Hivon, E., Huang, Z., Jaffe, A. H., Jones, W. C., Karakci, A., Keihänen, E., Keskitalo, R., Kiiveri, K., Kim, J., Kisner, T. S., Knox, L., Krachmalnicoff, N., Kunz, M., Kurki-Suonio, H., Lagache, G., Lamarre, J. M., Lasenby, A., Lattanzi, M., Lawrence, C. R., Le Jeune, M., Lemos, P., Lesgourgues, J., Levrier, F., Lewis, A., Liguori, M., Lilje, P. B., Lilley, M., Lindholm, V., López-Caniego, M., Lubin, P. M., Ma, Y. Z., Macías-Pérez, J. F., Maggio, G., Maino, D., Mandolesi, N., Mangilli, A., Marcos-Caballero, A., Maris, M., Martin, P. G., Martinelli, M., Martínez-González, E., Matarrese, S., Mauri, N., McEwen, J. D., Meinhold, P. R., Melchiorri, A., Mennella, A., Migliaccio, M., Millea, M., Mitra, S., Miville-Deschênes, M. A., Molinari, D., Montier, L., Morgante, G., Moss, A., Natoli, P., Nørgaard-Nielsen, H. U., Pagano, L., Paoletti, D., Partridge, B., Patanchon, G., Peiris, H. V., Perrotta, F., Pettorino, V., Piacentini, F., Polastri, L., Polenta, G., Puget, J. L., Rachen, J. P., Reinecke, M., Remazeilles, M., Renzi, A., Rocha, G., Rosset, C., Roudier, G., Rubiño-Martín, J. A., Ruiz-Granados, B., Salvati, L., Sandri, M., Savelainen, M., Scott, D., Shellard, E. P. S., Sirignano, C., Sirri, G., Spencer, L. D., Sunyaev, R., Suur-Uski, A. S., Tauber, J. A., Tavagnacco, D., Tenti, M., Toffolatti, L., Tomasi, M., Trombetti, T., Valenziano, L., Valiviita, J., Van Tent, B., Vibert, L., Vielva, P., Villa, F., Vittorio, N., Wandelt, B. D., Wehus, I. K., White, M., White, S. D. M., Zacchei, A., and Zonca, A. (2020). Planck 2018 results. VI. Cosmological parameters. , 641:A6.

Polzin, A., van Dokkum, P., Danieli, S., Greco, J. P., and Romanowsky, A. J. (2021). A Recently Quenched Isolated Dwarf Galaxy Outside of the Local Group Environment. , 914(1):L23.

Pontzen, A. and Governato, F. (2012). How supernova feedback turns dark matter cusps into cores. , 421(4):3464–3471.

Press, W. H. and Schechter, P. (1974). Formation of Galaxies and Clusters of Galaxies by Self-Similar Gravitational Condensation. , 187:425–438.

Quinn, T., Katz, N., and Efstathiou, G. (1996). Photoionization and the formation of dwarf galaxies. , 278(4):L49–L54.

Read, J. I. and Gilmore, G. (2005). Mass loss from dwarf spheroidal galaxies: the origins of shallow dark matter cores and exponential surface brightness profiles. , 356(1):107–124.

Read, J. I., Iorio, G., Agertz, O., and Fraternali, F. (2017). The stellar mass-halo mass relation of isolated field dwarfs: a critical test of ΛCDM at the edge of galaxy formation. , 467(2):2019–2038.

Rees, M. J. (1986). Lyman absorption lines in quasar spectra: evidence for gravitationally-confined gas in dark minihaloes. , 218(1):25P–30P.

Rey, M. P., Pontzen, A., Agertz, O., Orkney, M. D. A., Read, J. I., and Rosdahl, J. (2020). EDGE: from quiescent to gas-rich to star-forming low-mass dwarf galaxies. , 497(2):1508–1520.

Rey, M. P., Pontzen, A., Agertz, O., Orkney, M. D. A., Read, J. I., Saintonge, A., Kim, S. Y., and Das, P. (2022). EDGE: What shapes the relationship between H I and stellar observables in faint dwarf galaxies? , 511(4):5672–5681.

Ricotti, M. (2009). Late gas accretion on to primordial minihaloes: a model for Leo T, dark galaxies and extragalactic high-velocity clouds. , 392(1):L45–L49.

Ricotti, M. and Gnedin, N. Y. (2005). Formation Histories of Dwarf Galaxies in the Local Group. , 629(1):259–267.

Ricotti, M., Gnedin, N. Y., and Shull, J. M. (2001). Feedback from Galaxy Formation: Production and Photodissociation of Primordial H_2. , 560(2):580–591.

Rosswog, S. (2009). Astrophysical smooth particle hydrodynamics. , 53(4-6):78–104.

Rubin, V. C. and Ford, W. Kent, J. (1970). Rotation of the Andromeda Nebula from a Spectroscopic Survey of Emission Regions. , 159:379.

Sales, L. V., Navarro, J. F., Abadi, M. G., and Steinmetz, M. (2007). Cosmic ménage à trois: the origin of satellite galaxies on extreme orbits. , 379(4):1475–1483.

Sand, D. J., Mutlu-Pakdil, B., Jones, M. G., Karunakaran, A., Wang, F., Yang, J., Chiti, A., Bennet, P., Crnojević, D., and Spekkens, K. (2022). Tucana B: An Isolated and Quenched Ultra-faint Dwarf Galaxy at D=1.4 Mpc. *arXiv e-prints*, page arXiv:2205.09129.

Sawala, T., Frenk, C. S., Fattahi, A., Navarro, J. F., Bower, R. G., Crain, R. A., Dalla Vecchia, C., Furlong, M., Helly, J. C., Jenkins, A., Oman, K. A., Schaller, M., Schaye, J., Theuns, T., Trayford, J., and White, S. D. M. (2016). The APOSTLE simulations: solutions to the Local Group's cosmic puzzles. , 457(2):1931–1943.

Schaye, J. (2004). Star Formation Thresholds and Galaxy Edges: Why and Where. , 609(2):667–682.

Schaye, J., Crain, R. A., Bower, R. G., Furlong, M., Schaller, M., Theuns, T., Dalla Vecchia, C., Frenk, C. S., McCarthy, I. G., Helly, J. C., Jenkins, A., Rosas-Guevara, Y. M., White, S. D. M., Baes, M., Booth, C. M., Camps, P., Navarro, J. F., Qu, Y., Rahmati, A., Sawala, T., Thomas, P. A., and Trayford, J. (2015). The EAGLE project: simulating the evolution and assembly of galaxies and their environments. , 446(1):521–554.

Shapiro, P. R., Giroux, M. L., and Babul, A. (1994). Reionization in a Cold Dark Matter Universe: The Feedback of Galaxy Formation on the Intergalactic Medium. , 427:25.

Skillman, E. D., Monelli, M., Weisz, D. R., Hidalgo, S. L., Aparicio, A., Bernard, E. J., Boylan-Kolchin, M., Cassisi, S., Cole, A. A., Dolphin, A. E., Ferguson, H. C., Gallart, C., Irwin, M. J., Martin, N. F., Martínez-Vázquez, C. E., Mayer, L., McConnachie, A. W., McQuinn, K. B. W., Navarro, J. F., and Stetson, P. B. (2017). The ISLAndS Project. II. The Lifetime Star Formation Histories of Six Andomeda dSphS. , 837(2):102.

Skinner, D. and Wise, J. H. (2020). Cradles of the first stars: self-shielding, halo masses, and multiplicity. , 492(3):4386–4397.

Somerville, R. S. (2002). Can Photoionization Squelching Resolve the Substructure Crisis? , 572(1):L23–L26.

Somerville, R. S. and Davé, R. (2015). Physical Models of Galaxy Formation in a Cosmological Framework. , 53:51–113.

Springel, V. (2010). Smoothed Particle Hydrodynamics in Astrophysics. , 48:391–430.

Springel, V., Pakmor, R., Pillepich, A., Weinberger, R., Nelson, D., Hernquist, L., Vogelsberger, M., Genel, S., Torrey, P., Marinacci, F., and Naiman, J. (2018).

First results from the IllustrisTNG simulations: matter and galaxy clustering. , 475(1):676–698.

Springel, V., Wang, J., Vogelsberger, M., Ludlow, A., Jenkins, A., Helmi, A., Navarro, J. F., Frenk, C. S., and White, S. D. M. (2008). The Aquarius Project: the subhaloes of galactic haloes. , 391(4):1685–1711.

Springel, V., White, S. D. M., Jenkins, A., Frenk, C. S., Yoshida, N., Gao, L., Navarro, J., Thacker, R., Croton, D., Helly, J., Peacock, J. A., Cole, S., Thomas, P., Couchman, H., Evrard, A., Colberg, J., and Pearce, F. (2005). Simulations of the formation, evolution and clustering of galaxies and quasars. , 435(7042):629–636.

Springel, V., White, S. D. M., Tormen, G., and Kauffmann, G. (2001). Populating a cluster of galaxies - I. Results at [formmu2]z=0. , 328(3):726–750.

Tegmark, M., Silk, J., Rees, M. J., Blanchard, A., Abel, T., and Palla, F. (1997). How Small Were the First Cosmological Objects? , 474:1.

Teyssier, M., Johnston, K. V., and Kuhlen, M. (2012). Identifying Local Group field galaxies that have interacted with the Milky Way. , 426(3):1808–1818.

Theuns, T., Leonard, A., Efstathiou, G., Pearce, F. R., and Thomas, P. A. (1998). P$\hat{3}$M-SPH simulations of the Lyalpha forest. , 301(2):478–502.

Thoul, A. A. and Weinberg, D. H. (1996). Hydrodynamic Simulations of Galaxy Formation. II. Photoionization and the Formation of Low-Mass Galaxies. , 465:608.

Tollet, E., Macciò, A. V., Dutton, A. A., Stinson, G. S., Wang, L., Penzo, C., Gutcke, T. A., Buck, T., Kang, X., Brook, C., Di Cintio, A., Keller, B. W., and Wadsley, J. (2016). NIHAO - IV: core creation and destruction in dark matter density profiles across cosmic time. , 456(4):3542–3552.

Tolstoy, E., Hill, V., and Tosi, M. (2009). Star-Formation Histories, Abundances, and Kinematics of Dwarf Galaxies in the Local Group. , 47(1):371–425.

Vogelsberger, M., Marinacci, F., Torrey, P., and Puchwein, E. (2020). Cosmological simulations of galaxy formation. *Nature Reviews Physics*, 2(1):42–66.

Wang, L., Dutton, A. A., Stinson, G. S., Macciò, A. V., Penzo, C., Kang, X., Keller, B. W., and Wadsley, J. (2015). NIHAO project - I. Reproducing the inefficiency of galaxy formation across cosmic time with a large sample of cosmological hydrodynamical simulations. , 454(1):83–94.

Watkins, L. L., Evans, N. W., and An, J. H. (2010). The masses of the Milky Way and Andromeda galaxies. , 406(1):264–278.

Weisz, D. R., Dalcanton, J. J., Williams, B. F., Gilbert, K. M., Skillman, E. D., Seth, A. C., Dolphin, A. E., McQuinn, K. B. W., Gogarten, S. M., Holtzman, J., Rosema, K., Cole, A., Karachentsev, I. D., and Zaritsky, D. (2011). The ACS Nearby Galaxy Survey Treasury. VIII. The Global Star Formation Histories of 60 Dwarf Galaxies in the Local Volume. , 739(1):5.

Weisz, D. R., Dolphin, A. E., Skillman, E. D., Holtzman, J., Gilbert, K. M., Dalcanton, J. J., and Williams, B. F. (2014a). The Star Formation Histories of Local Group Dwarf Galaxies. I. Hubble Space Telescope/Wide Field Planetary Camera 2 Observations. , 789(2):147.

Weisz, D. R., Dolphin, A. E., Skillman, E. D., Holtzman, J., Gilbert, K. M., Dalcanton, J. J., and Williams, B. F. (2014b). The Star Formation Histories of Local Group Dwarf Galaxies. II. Searching For Signatures of Reionization. , 789(2):148.

Wheeler, C., Hopkins, P. F., Pace, A. B., Garrison-Kimmel, S., Boylan-Kolchin, M., Wetzel, A., Bullock, J. S., Kereš, D., Faucher-Giguère, C.-A., and Quataert, E. (2019). Be it therefore resolved: cosmological simulations of dwarf galaxies with 30 solar mass resolution. , 490(3):4447–4463.

White, S. D. M. and Frenk, C. S. (1991). Galaxy Formation through Hierarchical Clustering. , 379:52.

White, S. D. M. and Rees, M. J. (1978). Core condensation in heavy halos: a two-stage theory for galaxy formation and clustering. , 183(3):341–358.

Whiting, A. B., Hau, G. K. T., and Irwin, M. (1999). A New Local Group Galaxy in Cetus. , 118(6):2767–2774.

Wiersma, R. P. C., Schaye, J., and Smith, B. D. (2009). The effect of photoionization on the cooling rates of enriched, astrophysical plasmas. , 393(1):99–107.

Wright, A. C., Brooks, A. M., Weisz, D. R., and Christensen, C. R. (2019). Reignition of star formation in dwarf galaxies. , 482(1):1176–1189.

Appendix A

Star-formation classification

This appendix describes how the star-formation/quiescent classification was recovered from the different references used in producing the bottom panel of Fig. 4.6. The classification consistent was consistent with the definition used for the APOSTLE simulations, where any galaxy that showed evidence of star-formation within 0.5 Gyr of present day were labelled as star-forming.

This was straightforward to implement for Jeon et al. (2017) and Wheeler et al. (2019), which provided the star-formation histories of their simulated galaxies. See Fig. A.1 for an example of the dwarf galaxy SFH provided, where the green and pink galaxies were the only ones labeled star-forming.

For Rey et al. (2022), the star-forming classification were provided in the paper: star-forming galaxies have SFR of $\sim 10^{-5} M_{\odot} \mathrm{yr}^{-1}$, and the quiescent galaxies have not experience any star-formation since $z \sim 4$. This classification is broadly in line with the classification used for the APOSTLE simulation

For Fitts et al. (2017), the method employed was not as robust. Here we used the cumulative stellar mass (CSM) history shown Fig. A.2. The CSM of two galaxies reached the terminal value of 1 before $z = 0$, while all other galaxies continued forming stars until present day. The corresponding halo and stellar mass of these quiescent galaxies was recovered from their Table. 1, because only two of their galaxies had no cold-gas remaining. The remaining galaxies were labeled star-forming.

For Wright et al. (2019), the CSM (shown in Fig. A.3) was used in conjunction with their classification of star-formation histories (dead, stripped, gappy, and continuous). Dead and stripped galaxies all reached the terminal value of 1 in their CSM prior to $z = 0$, and are labelled quiescent. All continuous galaxies only reach CSM=1 at present day, so they are labelled star-forming. Two of their gappy CSM are seen

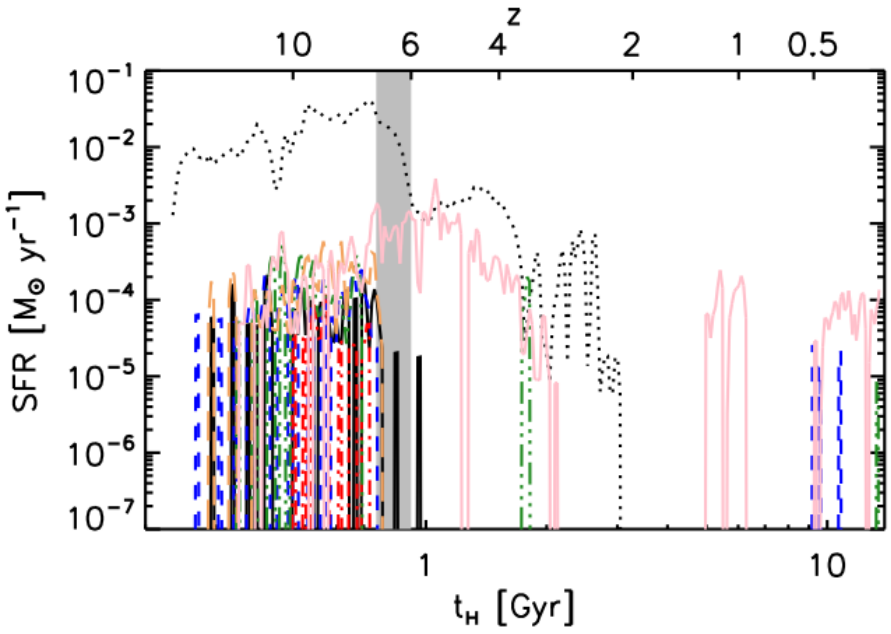

Figure A.1: Star-formation histories of dwarf galaxies from the Jeon et al. (2017) cosmological simulation. Only the green and pink galaxies are labeled star-forming under our classification scheme.

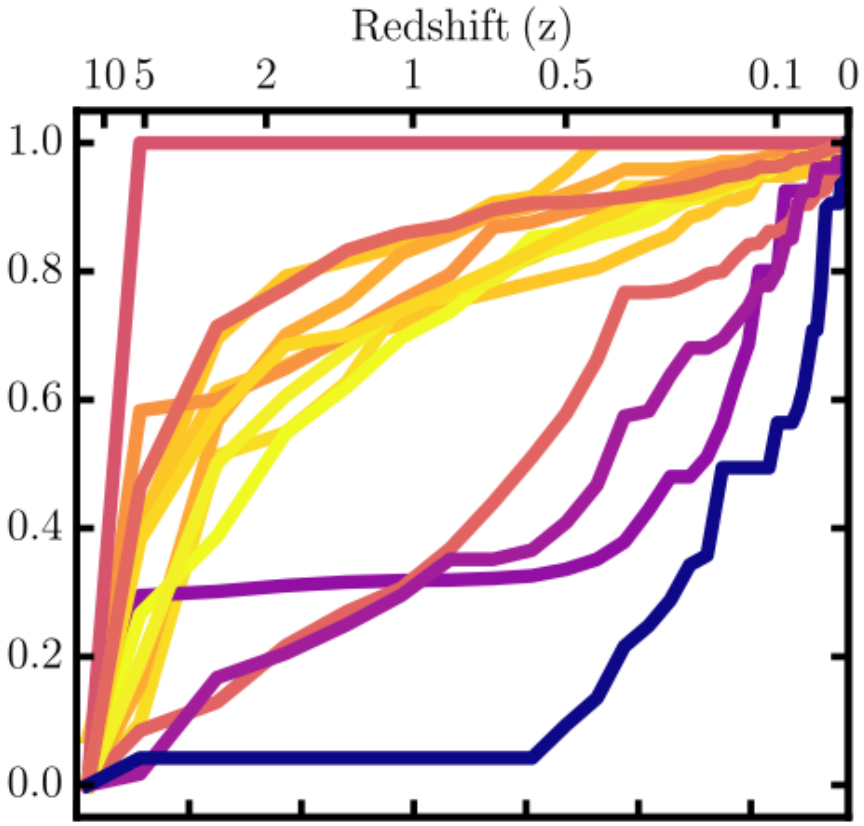

Figure A.2: Cumulative stellar mass formation history of dwarf galaxies form Fitts et al. (2017).

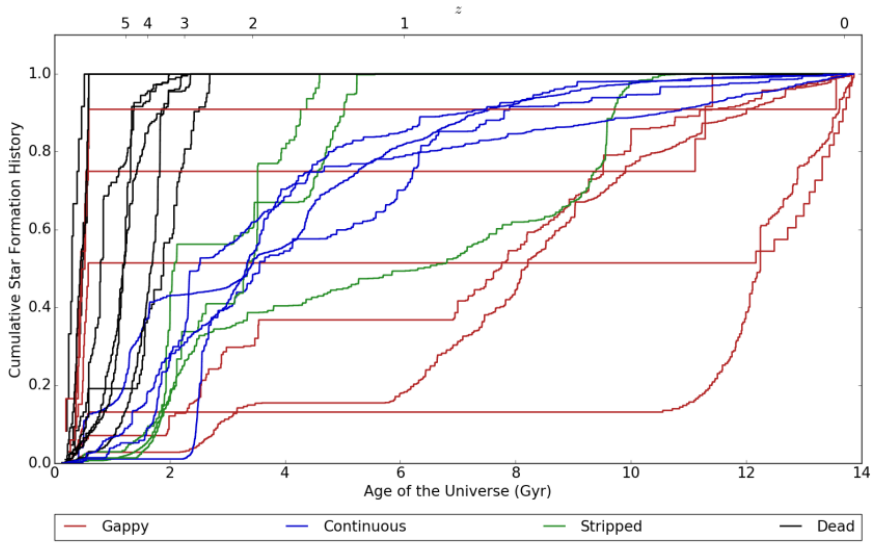

Figure A.3: Cumulative stellar mass formation history of dwarf galaxies form Wright et al. (2019).

reaching the CSM=1 value prior to $z = 0$, so they are labelled quiescent, while the remaining 4 of the same classification at labelled star-forming.